Article

Neurons that regulate mouse torpor

https://doi.org/10.1038/s41586-020-2387-5

Received: 22 January 2020

Accepted: 7 May 2020

Published online: 11 June 2020

Check for updates

Sinisa Hrvatin[1,6]✉, Senmiao Sun[1,2,6], Oren F. Wilcox[1], Hanqi Yao[1], Aurora J. Lavin-Peter[1], Marcelo Cicconet[3], Elena G. Assad[1], Michaela E. Palmer[1], Sage Aronson[4], Alexander S. Banks[5], Eric C. Griffith[1] & Michael E. Greenberg[1]✉

The advent of endothermy, which is achieved through the continuous homeostatic regulation of body temperature and metabolism[1,2], is a defining feature of mammalian and avian evolution. However, when challenged by food deprivation or harsh environmental conditions, many mammalian species initiate adaptive energy-conserving survival strategies—including torpor and hibernation—during which their body temperature decreases far below its homeostatic set-point[3–5]. How homeothermic mammals initiate and regulate these hypothermic states remains largely unknown. Here we show that entry into mouse torpor, a fasting-induced state with a greatly decreased metabolic rate and a body temperature as low as 20 °C[6], is regulated by neurons in the medial and lateral preoptic area of the hypothalamus. We show that restimulation of neurons that were activated during a previous bout of torpor is sufficient to initiate the key features of torpor, even in mice that are not calorically restricted. Among these neurons we identify a population of glutamatergic *Adcyap1*-positive cells, the activity of which accurately determines when mice naturally initiate and exit torpor, and the inhibition of which disrupts the natural process of torpor entry, maintenance and arousal. Taken together, our results reveal a specific neuronal population in the mouse hypothalamus that serves as a core regulator of torpor. This work forms a basis for the future exploration of mechanisms and circuitry that regulate extreme hypothermic and hypometabolic states, and enables genetic access to monitor, initiate, manipulate and study these ancient adaptations of homeotherm biology.

Torpor and hibernation enable warm-blooded animals to survive harsh environments that are otherwise incompatible with life[7,8]. Although constituting complex multifaceted behaviours[9–11], perhaps the most notable feature of these states is the profound decrease in core body temperature to far below its tightly controlled homeostatic set-point[3,4]. Several regions in the mammalian brain—including the preoptic area (POA)[12], the dorsomedial hypothalamus[13] and the raphe nuclei[14]—have been implicated in the coordination of temperature regulation[2]. Specific electrophysiologically and/or molecularly defined cellular components of homeostatic thermoregulation have been identified, including neurons that are sensitive to changes in ambient temperatures[15–18] and/or local brain temperature[19–21]. However, although a picture of the circuitry that underpins normal thermoregulation is beginning to emerge[1,2], how animals disengage or circumvent these conserved homeostatic mechanisms in response to environmental challenges to enter profoundly hypothermic states such as torpor and hibernation remains a central question in homeotherm biology.

To study the mechanisms that underlie the initiation of these adaptive hypothermic states, we used a model of fasting-induced torpor in laboratory mice (*Mus musculus*). Mice placed in environments that are devoid of food and are colder than their thermoneutral point (around 30 °C)[22,23] alternate between two survival strategies: high-risk food-seeking behaviour[24] and energy-conserving torpor[5,6,25]. Mouse torpor is a complex natural behaviour that is characterized by repeated bouts of profoundly reduced core body temperature (as low as 20 °C), along with decreases in movement, sensory perception, breathing, heart rate and metabolic rate[4–6,10,26–28]. To study fasting-induced torpor, mice were housed at 22 °C and implanted with telemetric temperature probes. Whereas fed mice maintained a core body temperature (T_b) higher than 35.1 ± 0.2 °C, all mice that were food-restricted for 24 hours experienced one or more bouts of torpor, which we characterized as a precipitous drop in core body temperature (greater than 1 °C per 20 min), a period of deep hypothermia (T_b of 24–35 °C) lasting up to several hours, and finally, arousal from torpor (Fig. 1a). Each bout of torpor was preceded by a 45.1 ± 4.6% decrease in metabolic rate and was accompanied by reduced movement (73.4 ± 7.0% reduction; Fig. 1a–c, Extended Data Fig. 1a). Although circadian rhythms[28], leptin signalling[27,29], sympathetic nervous system activity and adipose tissue thermogenesis[26,30] have all been shown to modulate torpor, the mechanisms by which animals trigger and regulate this natural hypothermic state remain unknown.

[1]Department of Neurobiology, Harvard Medical School, Boston, MA, USA. [2]Program in Neuroscience, Harvard Medical School, Boston, MA, USA. [3]Image and Data Analysis Core, Harvard Medical School, Boston, MA, USA. [4]Neurophotometrics, Ltd., San Diego, CA, USA. [5]Division of Endocrinology, Diabetes and Metabolism, Beth Israel Deaconess Medical Center, Boston, MA, USA. [6]These authors contributed equally: Sinisa Hrvatin, Senmiao Sun. ✉e-mail: sinisa_hrvatin@hms.harvard.edu; michael_greenberg@hms.harvard.edu

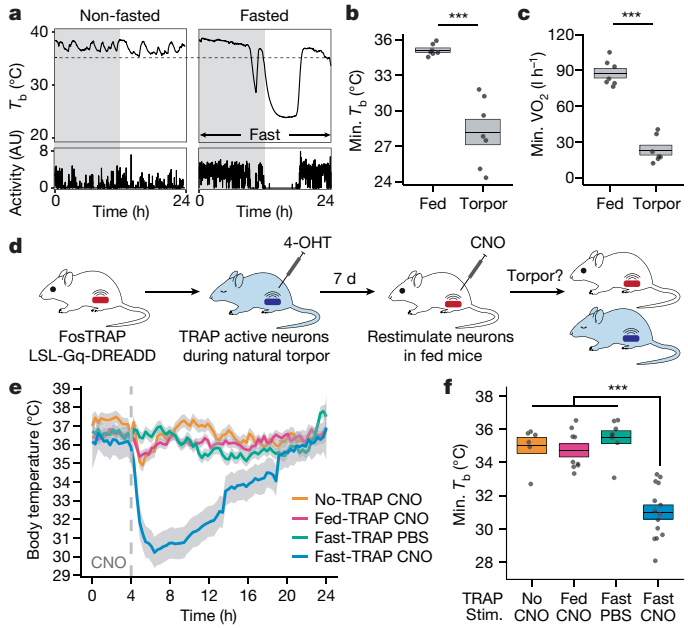

Fig. 1 | Neuronal activity induces key features of torpor. a, Core body temperature (T_b) and gross motor activity of a representative non-fasted (left) or fasted (right) mouse over 24 h. Fasted mice enter torpor, whereas non-fasted mice do not. The grey and white backgrounds indicate 12-h periods of darkness and light, respectively. The dashed line indicates the minimum T_b observed in non-fasted mice. **b**, **c**, Minimum T_b (**b**) and the minimum metabolic rate as measured by the volume of oxygen consumed (VO_2) (**c**) in non-fasted (fed) and fasted (torpor) mice ($n = 7$ mice, $^{***}P = 6 \times 10^{-4}$ (**b**), $^{***}P = 1 \times 10^{-5}$ (**c**)). **d**, Schematic showing the procedure for gaining genetic control over torpor-regulating neurons. Neurons active during torpor in FosTRAP, LSL-Gq-DREADD mice are TRAPed by 4-OHT administration and chemogenetically restimulated 7 days later in non-fasted mice by treatment with CNO. **e**, CNO-induced reactivation of 4-OHT-TRAPed neurons that are active during torpor entry triggers a decrease in T_b characteristic of mouse torpor (fast-TRAP CNO, $n = 14$ mice). The same mice injected with PBS (fast-TRAP PBS, $n = 8$ mice), or control mice in which neurons were not TRAPed (no-TRAP CNO, $n = 6$ mice) or were TRAPed during a non-torpid state (fed-TRAP CNO, $n = 9$ mice), did not show a decrease in T_b upon CNO administration. The dashed line indicates the onset of CNO or PBS administration, shading indicates 95% confidence interval. **f**, The minimum T_b after CNO administration is lower in fast-TRAP CNO ($n = 14$) mice compared to no-TRAP CNO ($n = 6$, $P = 6.2 \times 10^{-4}$), fed-TRAP CNO ($P = 2.4 \times 10^{-6}$) or fast-TRAP PBS ($P = 2.5 \times 10^{-5}$) mice. For the box plots, the centre line and box boundaries indicate mean ± s.e.m. *P* values were calculated using a two-tailed Mann–Whitney *U*-test, $^{***}P < 0.001$.

Torpor-associated circuit activity

In principle, entry into torpor could be triggered by circulating factors capable of reducing metabolic rate and/or by changes in thermoregulatory neural circuit activity. Consistent with the idea that altered circuit activity contributes to entry into torpor[26], staining for FOS—a marker of neuronal activity-induced transcription[31]—followed by whole-brain imaging and machine learning-enabled registration of the FOS signal to the Allen Mouse Brain Atlas[32] (Methods) revealed several brain regions that are active during fasting-induced torpor. As might be expected, we observed neuronal activity in brain regions that regulate hunger, feeding and energy balance[33,34], as well as in thermoregulatory areas[1,2,35] and in a large number of other brain regions. This finding that brain circuits are engaged as fasted mice enter torpor suggests that these circuits might potentially drive the entry process (Extended Data Fig. 1b–f).

To determine whether neural circuit activity is sufficient to induce torpor phenotypes independent of caloric restriction, we used genetic tools that enable the expression of a chemically activated receptor, Gq-DREADD (Gq-coupled Designer Receptor Exclusively Activated by Designer Drug), specifically in the neurons that are active as mice enter torpor. Reactivation of the putative torpor-regulating neurons by administration of the Gq-DREADD-activating synthetic ligand clozapine *N*-oxide (CNO) to the mice enabled us to determine whether the reactivation of these neurons alone—without caloric restriction—is sufficient to induce torpor-associated phenotypes. For this experiment, we used mice harbouring a tamoxifen-dependent form of Cre recombinase driven from the *Fos* locus ($Fos^{2A\text{-}iCreERT2}$, TRAP2[36]) together with an allele of the Gq-coupled receptor that is expressed in a Cre-dependent manner (R26-LSL-Gq-DREADD[37]). When these 'FosTRAP-Gq' mice are fasted to induce entry into torpor, the neurons that are active—and thus potentially mediate torpor entry—induce FOS and CreERT2. When these mice are exposed to 4-hydroxytamoxifen (4-OHT), the CreERT2 recombines the R26-LSL-Gq-DREADD allele, leading to the persistent expression of Gq-DREADD and enabling these specific neurons—referred to hereafter as 'TRAPed' neurons—to be activated at a later time by the administration of CNO (Fig. 1d).

FosTRAP-Gq mice ($n = 14$) were fasted and 4-OHT was administered as they entered natural torpor. After several days of recovery from fasting, these mice were administered the DREADD-activating ligand CNO to chemogenetically restimulate the neurons that were TRAPed during natural torpor (Fig. 1d, Methods). Notably, we found that the stimulation of neurons that were previously active during fasting and torpor was sufficient to induce the robust decrease in core body temperature and locomotor activity associated with natural torpor, despite the absence of caloric restriction. This effect was dependent on CNO administration and on previous 4-OHT-mediated TRAPing in the fasted state (Fig. 1e, f, Extended Data Fig. 1g, h). Although we cannot exclude a contribution either from fasting-regulated neurons that are active before or after torpor or from non-neuronal cells, this result suggests that the systemic recapitulation of torpor-associated neuronal circuit activity is sufficient to acutely induce key behavioural and physiological features of torpor.

avMLPA neurons regulate features of torpor

To identify the brain areas that were labelled using the TRAP approach, we immunostained brain sections of these FosTRAP-Gq mice for the haemagglutinin-tagged Gq-DREADD protein. Whole-brain imaging revealed widespread expression of the Gq-DREADD protein, with 190 differentially labelled regions identified between mice TRAPed in a fasted state (fast-TRAPed) compared with mice in a fed state (fed-TRAPed; Extended Data Fig. 1i–k, Supplementary Table 1). A strong correlation across brain regions was observed between the number of FOS^+ cells in torpid mice and the levels of Gq-DREADD expression in fast-TRAPed mice, suggesting that our TRAP approach labelled—as intended—neurons that are active and induce FOS during torpor (Extended Data Fig. 1l). Although in principle the simultaneous activation of multiple neural populations across several distributed brain areas might be required to orchestrate torpor, we proposed that circuit activity within a single brain region might have a major role in the regulation of torpor. To address this possibility, we designed a screen across the brain regions that were identified by Gq-DREADD staining in fast-TRAPed mice. By stereotactic injection into FosTRAP mice, which do not express an endogenous Gq-DREADD, we administered adeno-associated viruses (AAVs) expressing Cre-dependent Gq-DREADD fused to mCherry (AAV-DIO-Gq–mCherry); this enabled TRAPing restricted to the injection area, the expression of Gq-DREADD–mCherry, and the subsequent chemogenetic restimulation of the neurons active during natural torpor within just the injected region (Fig. 2a). For these studies, we focused on the torpor-associated decrease in core body temperature. We injected FosTRAP mice ($n = 54$) in different areas of the anterior hypothalamus, a region of the brain involved in thermoregulation and energy balance[1,2] that

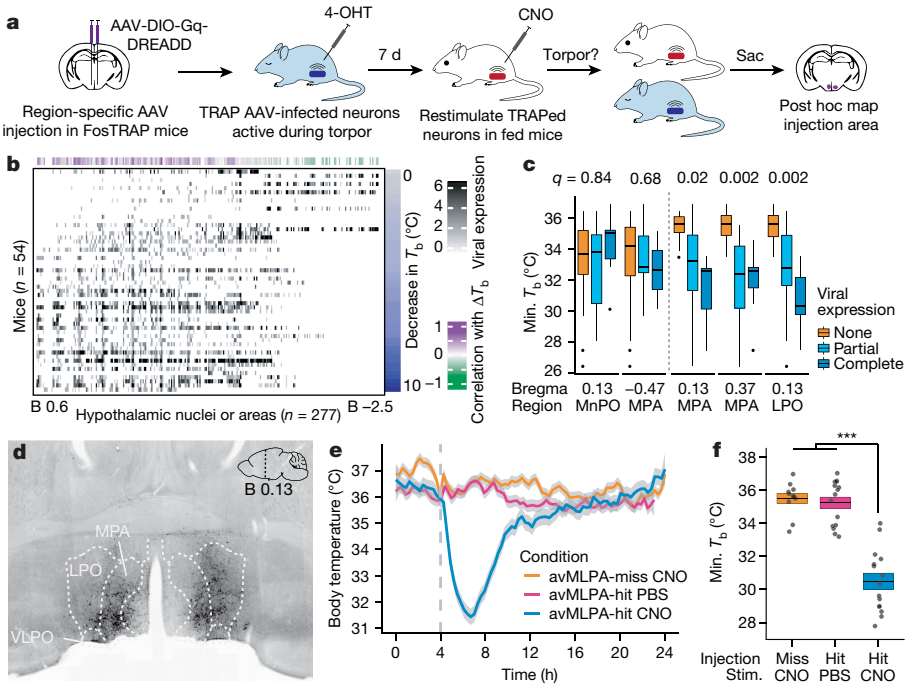

Fig. 2 | Identification of brain regions that regulate torpor. a, Schematic showing the procedure for identifying which hypothalamic regions contain torpor-regulating neurons. **b**, Quantification of AAV-DIO-Gq-DREADD–mCherry expression in mice TRAPed during fasting-induced torpor. Hypothalamic nuclei ($n = 277$) are plotted on the basis of their anterior–posterior (AP) coordinates relative to bregma (B). Mice ($n = 54$) are ranked on the basis of the decrease in core body temperature (ΔT_b) observed after chemogenetic stimulation of TRAPed neurons. ΔT_b is correlated with viral expression in each region (Pearson correlation). **c**, Two regions in which viral expression did not show significant correlation to ΔT_b (first two columns) and three regions in which viral expression did show significant correlation to ΔT_b (final three columns). False discovery rate (FDR)-corrected q value, Pearson correlation test, $n = 54$ mice. The minimum T_b was calculated across all mice grouped on the basis of degree of viral expression into 'none', 'partial' or 'complete'. In the box plots the centre line denotes the median, the box boundaries mark the interquartile range (IQR) and the whiskers extend to 1.5 × IQR. MnPO, median preoptic nucleus; MPA, medial preoptic area; LPO, lateral preoptic area. **d**, Representative coronal section from an avMLPA-injected mouse ($n = 15$ mice). VLPO, ventrolateral preoptic nucleus. **e**, **f**, Chemogenetic restimulation of avMLPA TRAPed neurons (avMLPA-hit CNO, $n = 15$ mice), the same mice ($n = 15$) injected with PBS (avMLPA-hit PBS), or control mice in which the avMLPA was missed (avMLPA-miss, $n = 11$ mice). **e**, A decrease in T_b characteristic of torpor is seen only in avMLPA-hit CNO mice. The dashed line indicates CNO or PBS administration, grey shading indicates 95% confidence interval of T_b. **f**, The minimum T_b after CNO administration is lower in avMLPA-hit mice compared with avMLPA-miss mice ($P = 1.8 \times 10^{-6}$) or with avMLPA-hit mice injected with PBS ($P = 5.8 \times 10^{-7}$). Two-tailed Mann–Whitney U-test, ***$P < 0.001$. For the box plots, the centre line and box boundaries indicate mean ± s.e.m.

showed substantial FOS expression during fasting-induced torpor (Extended Data Fig. 1). After recovery, these mice—hereafter denoted 'FosTRAP$^{AAV\text{-}Gq}$' mice—were fast/torpor-TRAPed, enabling persistent expression of the viral Cre-dependent Gq-DREADD–mCherry in fast- and torpor-active neurons within the virally injected region. Several days later, we administered CNO to stimulate Gq-DREADD-expressing neurons selectively in the injected region of the hypothalamus to test whether the stimulation of these neurons would result in a decrease in body temperature, as in natural torpor. The reduction of core body temperature was correlated with the anatomical expression of the virally derived Gq-DREADD–mCherry across 277 hypothalamic nuclei or areas (Fig. 2b, Methods). Leveraging the variability across injection sites in different mice ($n = 54$), this unbiased screen identified the anterior and ventral portions of the medial and lateral preoptic area (avMLPA) as key regions, with mice injected in the avMLPA exhibiting a large decrease in core body temperature in response to CNO as compared with mice in which these regions were not transduced (4.90 ± 0.68 °C compared with 0.89 ± 0.25 °C, $P = 1.8 \times 10^{-6}$; Fig. 2c–f, Extended Data Fig. 2a–c, Supplementary Tables 2, 3). FosTRAP$^{AAV\text{-}Gq}$ mice that were injected selectively in the avMLPA, TRAPed during torpor, allowed sufficient time to recover and then stimulated with CNO showed a decrease in metabolic rate of 30.4 ± 8.5% ($P < 2.4 \times 10^{-3}$) and a decrease in gross motor activity of 58.7 ± 5.2% ($P < 1.5 \times 10^{-3}$), consistent with the features observed in natural torpor (Extended Data Fig. 2d–g). Moreover, sectioning and staining brains for the virally derived Cre-dependent Gq-DREADD–mCherry fusion protein revealed projections from torpor-TRAPed avMLPA (avMLPA^{torpor}) neurons to the dorsomedial hypothalamus, arcuate nucleus, periaqueductal grey and raphe pallidus—regions that are known to modulate energy balance and adipose tissue thermogenesis, which are processes thought to be involved in the induction of torpor[38,39] (Extended Data Fig. 2h–j). Together, these findings identify a brain area in which the reactivation of torpor-associated neurons is sufficient to acutely induce torpor-like behavioural and physiological changes, and suggest that avMLPA^{torpor} neurons may represent a critical node in the circuit that regulates natural entry into torpor.

Molecular analysis of avMLPA^{torpor} neurons

The mammalian POA houses an interconnected ensemble of cell types that are involved in temperature[15–17,20], fluid[36] and cardiovascular homeostasis[40], as well as mating, parental behaviours[41] and sleep[42–44]. To catalogue the diversity of neuronal cell types present in the avMLPA, and identify which among them are active and TRAPed during torpor, we adapted a high-throughput single-nucleus RNA-sequencing (snRNA-seq)-based strategy[45] (Fig. 3a). Five FosTRAP mice were injected with AAV-DIO-Gq-DREADD–mCherry. Four of these mice were TRAPed during torpor, while one was kept as a non-TRAPed control. Their anteroventral POAs were dissected and dissociated, and 44,669 single nuclei

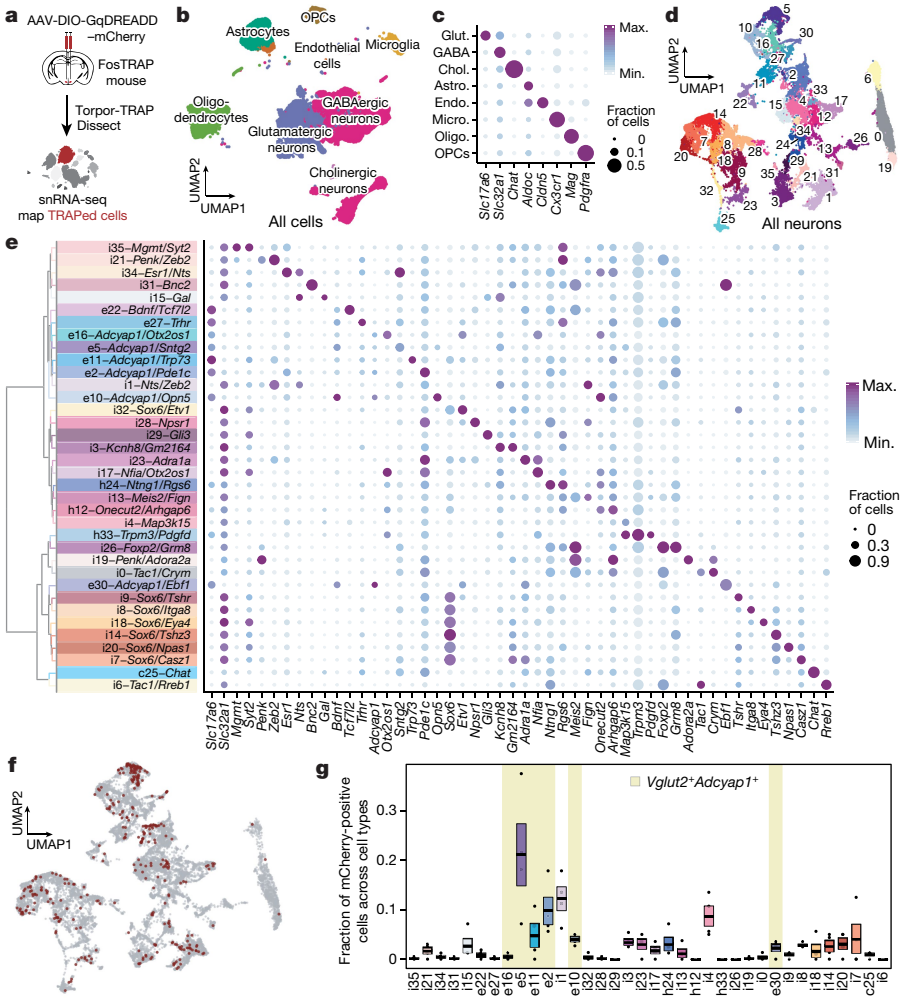

Fig. 3 | Molecular characterization of torpor-associated avMLPA neurons. **a**, Schematic showing the procedure for the molecular characterization of avMLPA^{torpor} cells. AAV-DIO-Gq-DREADD is injected into the avMLPA ($n = 5$ mice). After TRAPing, the avMLPA is microdissected and analysed by snRNA-seq. **b**, Uniform manifold approximation and projection (UMAP) plot of 39,562 nuclei from the avMLPA of 5 mice. Colours group the main cell types. OPCs, oligodendrocyte precursor cells. **c**, Expression of the indicated marker genes across different cell types (named as abbreviations of the cell types in **b**). **d**, UMAP plot of 28,103 neuronal nuclei. Colours group the 36 neuronal subtypes. **e**, Expression of marker genes across different neuronal cell types. Cell types are organized on the basis of hierarchical clustering. The acronym comprises the neuronal class (e, excitatory; i, inhibitory; h, hybrid; c, cholinergic) and the cluster number, followed by select marker genes. **f**, UMAP plot of 17,424 neuronal nuclei that were transduced by the AAV (grey) and 342 neuronal nuclei that were TRAPed during torpor (red). **g**, Distribution of TRAPed neurons across all neuronal cell types. For the box plots, the centre line and box boundaries indicate mean ± s.e.m. ($n = 4$ mice). Yellow shading indicates cell types expressing *Adcyap1* and *Vglut2*. The acronym comprises the neuronal class and the cluster number. In **c**, **e**, the colour of the circle denotes the mean expression across all nuclei normalized to the highest mean across cell types, and the size of the circle represents the fraction of nuclei in which the marker gene was detected.

were analysed using snRNA-seq at an average depth of 1,286 genes and 2,083 transcripts per nucleus (Extended Data Fig. 3a–e). Unsupervised graph-based clustering delineated major neuronal and non-neuronal cell classes, and further clustering of just the neuronal subpopulation ($n = 28,103$) identified a considerable diversity of 24 GABAergic, 8 glutamatergic, 3 hybrid (GABAergic and glutamatergic) and one cholinergic neuronal cell type, consistent with the large diversity of cell types present in the POA[41] (Fig. 3b–e, Extended Data Fig. 4, Supplementary Table 4). The robustness of the obtained clusters was confirmed by subsampling analysis (Extended Data Fig. 3f). Notably, 17,424 of the 28,103 sequenced neurons—representing all 36 cell types—expressed AAV-derived transcripts, consistent with broad tropism of AAV8 in the hypothalamus.

We analysed the expression of Gq-DREADD–mCherry transcripts as a means to identify which among the transduced neurons were TRAPed during torpor. This approach detected 342 torpor-TRAPed neurons among 15,056 transduced neurons in the four TRAPed mice, and displayed a low false-positive and false-negative rate (Extended Data Fig. 5a–e, Methods). TRAPed neurons represented several avMLPA cell types, suggesting that several neuronal populations were active during fasting-induced torpor (Fig. 3f). However, the largest subset (42.6 ± 3.5%) of all torpor-TRAPed cells consisted of several populations of glutamatergic *Adcyap1*$^+$ neurons (Fig. 3g, Extended Data Fig. 5f–i), a result that was subsequently confirmed using in situ hybridization methods (Extended Data Fig. 6, Extended Data Fig. 7). Differential gene expression analysis between TRAPed and non-TRAPed *Vglut2*$^+$*Adcyap1*$^+$ neurons identified markers of e5 neurons, consistent with preferential TRAPing of this molecularly defined subtype of *Adcyap1*$^+$ neurons (Supplementary Table 5).

Stimulation of torpor-associated neurons

Together with previous work that describes distinct populations of GABAergic and glutamatergic warm-sensitive thermoregulatory

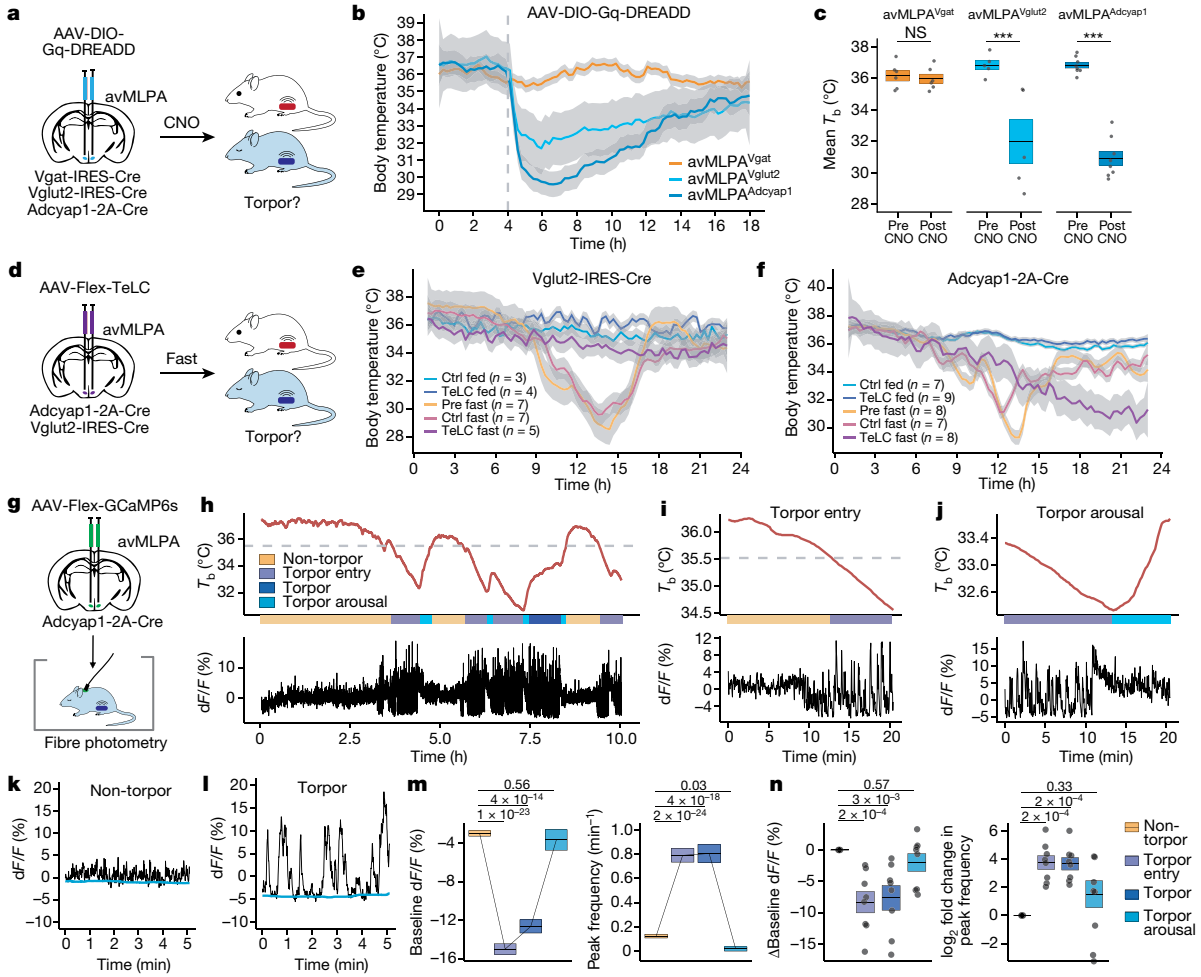

Fig. 4 | Sufficiency, necessity and natural activity of avMLPA neuronal subpopulations during torpor. a–**c**, The injection of AAV-DIO-Gq-DREADD and subsequent chemogenetic stimulation of avMLPA^{Vgat}, avMLPA^{Vglut2} and avMLPA^{Adcyap1} neurons ($n = 6$, 5 and 8 mice, respectively). **a**, Schematic showing the experimental procedure. **b**, Change in T_b after chemogenetic stimulation with CNO (indicated by the dashed line). **c**, Mean T_b before and after chemogenetic stimulation of avMLPA^{Vgat} (NS, $P = 0.48$), avMLPA^{Vglut2} (***$P = 7.9 \times 10^{-3}$), and avMLPA^{Adcyap1} neurons (***$P = 1.6 \times 10^{-4}$). **d**, Schematic showing the injection of AAV-Flex-TeLC to inhibit synaptic transmission. **e**, **f**, T_b of fed and fasted mice in which avMLPA^{Vglut2} (**e**) or avMLPA^{Adcyap1} (**f**) neurons remained un-injected (pre), were injected with a control AAV (ctrl), or were injected with AAV-Flex-TeLC (TeLC). Coloured lines indicate the mean across mice; grey shading indicates the 95% confidence interval. The number of mice for each condition is indicated in parentheses. **g**, Schematic showing the injection of AAV-Flex-GCaMP6s and fibre photometry recording from avMLPA^{Adcyap1} neurons. **h**–**j**, Recording sessions in fasted mice showing T_b and the normalized GCaMP6s signal. Coloured bars indicate the different states, classified on the basis of T_b. The dashed line indicates the transition between non-torpor and torpor states (Methods). F denotes the fluorescence intensity of GCaMP6s, and dF/F is calculated by dividing the smoothed calcium-dependent GCaMP6s signal with the Ca^{2+}-independent scaled fit. **h**, Example 10-h trace spanning non-torpor and torpor states. **i**, **j**, Example 20-min traces spanning torpor entry (**i**) and torpor arousal (**j**). **k**, **l**, Example photometry signals in non-torpor (**k**) and torpor (**l**) states. The baseline signal is indicated in blue. **m**, Mean baseline (left) and peak frequency (right) of the fibre photometry signal in one mouse across non-torpor and torpor states. The legend is displayed in **n**, and P values are indicated above the plots. **n**, Difference in average baseline (left) and $\log_2$ fold change in average peak frequency (right) of fibre photometry signal between non-torpor and torpor states ($n = 8$ mice, P values indicated above plots). For the box plots, the centre line and box boundaries indicate mean ± s.e.m. All P values were calculated using a two-tailed Mann–Whitney U-test.

neurons in the POA[16–18,46], our results suggest the possibility that avMLPA neurons that express *Vglut2* or *Adcyap1* (avMLPA^{Vglut2} and avMLPA^{Adcyap1} neurons, respectively) regulate the decrease in core body temperature that is associated with natural torpor. To directly test whether stimulation of these neurons is sufficient to phenocopy the decrease in body temperature observed during natural torpor, we used Vglut2-IRES-Cre and Adcyap1-2A-Cre mice and expressed the excitatory Gq-DREADD in avMLPA^{Vglut2} or avMLPA^{Adcyap1} neurons (Fig. 4a). Chemogenetic activation of avMLPA^{Adcyap1} or avMLPA^{Vglut2} neurons resulted in a rapid decrease in core body temperature (5.9 ± 0.4 °C and 4.9 ± 1.0 °C, respectively) and in gross motor activity (58.7 ± 8.4% and 53.3 ± 11.8%, respectively; Fig. 4a–c, Extended Data Fig. 8a–f), which phenocopied the stimulation of torpor-TRAPed avMLPA neurons and effectively recapitulated the decrease in core body temperature and activity observed during natural torpor. By contrast, the chemogenetic activation of avMLPA^{Vgat} neurons in Vgat-IRES-Cre mice led to no significant change in core body temperature (0.2 ± 0.3 °C, $P = 0.48$, Fig. 4a–c, Extended Data Fig. 8b).

Silencing of torpor-associated neurons

Although these findings are consistent with the idea that torpor-active avMLPA^{Adcyap1} and avMLPA^{Vglut2} cells are critical torpor-inducing neurons in the avMLPA, it remained possible that these cells simply constituted a part of the core circuitry that controls homeostatic body temperature,

rather than being mediators of torpor entry. To directly address the role of avMLPA^{Adcyap1} and avMLPA^{Vglut2} neuronal activity in basal homeostatic thermoregulation, as well as the natural process of fasting-induced torpor, we targeted the expression of a virally encoded, Cre-dependent tetanus toxin light chain[47] (AAV-Flex-TeLC)—a derivative of a potent neurotoxin that eliminates synaptic transmission—to avMLPA^{Adcyap1} or avMLPA^{Vglut2} neurons (Fig. 4d). By expressing Gq-DREADD and TeLC in the same neurons and stimulating them with CNO, we were able to first verify that TeLC expression effectively inhibited synaptic transmission in these cells, to the extent that it blocked the decrease in core body temperature associated with the chemogenetic stimulation (Extended Data Fig. 8g–i). Experiments with fed mice showed that avMLPA^{Adcyap1} or avMLPA^{Vglut2} silencing had no significant effect on normal homeostatic body temperature, including its circadian rhythm (Fig. 4e, f, Extended Data Fig. 8j–o). By contrast, mice in which avMLPA^{Vglut2} neurons were selectively silenced showed profound disruption of fasting-induced torpor (Fig. 4e). Specifically, the decrease in core body temperature associated with fasting-induced torpor was significantly diminished after the injection of AAV-Flex-TeLC, as compared with that observed in the same mice before injection (pre-fast, $P = 0.010$) or in mice injected with a control AAV vector (control fast, $P = 0.018$, Extended Data Fig. 8j). The kinetics of the torpor-associated decrease in body temperature were also significantly altered by avMLPA^{Vglut2} silencing: mice reached their lowest body temperature after 22 ± 1 h, compared with 14 ± 1 h for control mice (Extended Data Fig. 8k, $P = 9.2 \times 10^{-3}$). Silencing of avMLPA^{Adcyap1} neurons—a subset of avMLPA^{Vglut2} neurons—also altered natural torpor (Fig. 4f, Extended Data Fig. 8l): normal torpor bouts were replaced with a gradual decrease in core body temperature, and an additional 6 h was required to reach a similar degree of hypothermia compared with normal torpor (Extended Data Fig. 8m, $P < 7 \times 10^{-3}$). It must be noted that the injected site in some cases included areas that extended beyond the avMLPA. In addition, using in situ hybridization techniques, we found that only a subset (43 ± 5%) of avMLPA *Adcyap1*$^+$ neurons expressed TeLC, perhaps due to inefficient viral transduction or Cre-mediated recombination. This may have led to the incomplete silencing of torpor-regulating avMLPA^{Adcyap1} neurons, and could be a reason for the incomplete elimination of fasting-induced torpor responses that we observed in this paradigm (Extended Data Fig. 8p, q). Nevertheless, these results suggest that the activity of avMLPA^{Adcyap1} neurons is necessary for the normal pattern of torpor thermoregulation—characterized by a rapid decrease in core body temperature, its maintenance and subsequent re-warming—and that, perhaps together with other glutamatergic neurons, avMLPA^{Adcyap1} neurons are required for the depth of hypothermia that is observed during natural torpor.

Dynamics of avMLPA^{Adcyap1} neurons in torpor

Active involvement of glutamatergic *Adcyap1*$^+$ avMLPA neurons in the initiation of torpor should be reflected by acute torpor-associated changes in avMLPA^{Adcyap1} neuronal firing patterns. Moreover, the characterization of avMLPA neuronal firing patterns during natural torpor might provide further insight into the underlying functional role of this circuit in torpor regulation. For example, natural avMLPA firing patterns might encode a caloric deficit, circadian time, rate of change in body temperature, time of acute torpor onset or maintenance of torpor. To distinguish between these possibilities, we expressed the calcium reporter[48] GCaMP6s in avMLPA^{Adcyap1} neurons, installed an optical fibre in the region containing these neurons, and continuously monitored neuronal calcium transients over 7–12 h in freely moving fasted mice as they entered torpor (Fig. 4g, Extended Data Fig. 9a, b, Methods). This analysis did not show a gradual change in neuronal activity correlated with caloric restriction or circadian time, or a transient pattern of activity that correlated with only the onset of torpor. Instead, we observed a marked change in neuronal activity that coincided with torpor entry and persisted until the mice began to exit the torpid state (Fig. 4h–l, Extended Data Fig. 9c, d, Methods). This torpor-associated activity pattern was characterized by an 8.0 ± 1.8% decrease in the baseline signal ($P = 3 \times 10^{-3}$) and a 19.0 ± 7.0-fold increase in the frequency of highly prominent Ca^{2+}-dependent peaks ($P = 2 \times 10^{-4}$, Fig. 4m, n, Extended Data Fig. 9d–g) compared with the non-torpor state. Notably, this distinct pattern of avMLPA^{Adcyap1} neuronal activity alone was sufficient to accurately model and determine when mice entered, maintained and exited torpor (Extended Data Fig. 9h–k), which suggests that avMLPA^{Adcyap1} neurons encode information specific to torpor entry and maintenance.

To exclude the possibility that the avMLPA^{Adcyap1} neurons were merely responding to an acute change in body temperature, we recorded their activity in fed mice in which hypothermia had been artificially induced by administration of the adenosine receptor agonist N^6-cyclohexyladenosine (CHA)[49]. Chemically induced hypothermia resulted in a similar decrease in baseline signal (7.2 ± 1.7%) to that seen in torpor, perhaps due to decreased neuronal discharge at lower body temperature. However, chemically induced hypothermia failed to produce the prominent Ca^{2+}-dependent peaks that are associated with fasting-induced torpor, suggesting that the large Ca^{2+} transients observed in avMLPA^{Adcyap1} neurons may encode information that is relevant specifically to torpor and not simply to hypothermia or cooling (Extended Data Fig. 10a–e). Whether this pattern of Ca^{2+} transients reflects the existence of distinct neuronal subpopulations—or perhaps burst firing of a single population of responsive neurons—remains unclear, as does its function in the process of torpor entry.

To investigate whether torpor-active avMLPA^{Adcyap1} neurons are distinct from previously identified populations of warm-sensitive neurons in the POA[16–18,46], we next challenged the mice in which we had previously observed torpor-related avMLPA^{Adcyap1} neuronal activity with either warm (37 °C) or cold (10 °C) environments. Unlike previously described warm-sensitive neurons, avMLPA^{Adcyap1} neurons showed no significant changes in activity in the warm environment; however, they did display sensitivity to a cold environment, suggesting the existence of several functionally distinct subpopulations of POA^{Adcyap1} neurons (Extended Data Fig. 10f–i). In summary, we show that avMLPA^{Adcyap1} neurons both contribute to and are necessary for the natural decrease in body temperature that is observed during torpor, and encode a unique pattern of broad and highly prominent Ca^{2+} transients as mice enter and sustain torpor. This suggests that the activity of these neurons is critical to the natural process of torpor initiation and maintenance in mice.

Discussion

Our study examines the mechanisms underlying a complex naturalistic behaviour by using several recent technological advances, including the FosTRAP approach, machine learning-enabled image registration, snRNA-seq and long-term recordings of neuronal activity. We implicate specific neuronal cell types within a defined brain region in the regulation of torpor, one of the most extreme and poorly understood physiological adaptations in homeothermic animals. We discover that neural activity alone is sufficient to induce several key features of torpor, including decreased locomotion and a profoundly lowered metabolic rate and core body temperature in mice that are not calorically restricted. We identify the avMLPA of the hypothalamus as a torpor control centre, and *Vglut2*$^+$*Adcyap1*$^+$ neurons as a central torpor-regulating neuronal population. We observe that the activity of these neurons changes markedly when mice naturally enter torpor, and that this both contributes to and is necessary for the precipitous decrease in core body temperature that is observed during natural torpor. How these torpor-regulating neurons integrate information about internal states and environmental experience remains to be understood. Glutamatergic avMLPA^{Adcyap1} neurons receive information about decreasing ambient temperatures, leading us to speculate that these neurons might integrate information about environmental conditions with information about the internal energy reserves of the animal, so as to

control when the animal enters torpor. Transcriptome-wide analysis of *Vglut2*$^{+}$*Adcyap1*$^{+}$ neurons identified expression of the leptin receptor in two of the *Vglut2*$^{+}$*Adcyap1*$^{+}$ neuronal subtypes, suggesting the possibility that circulating leptin levels might modulate the activity of torpor-regulating neurons and provide a potential mechanism for how information about decreased energy reserves in fasted mice could be conveyed to torpor-regulating avMLPA$^{Vglut2/Adcyap1}$ neurons[27,30] (Extended Data Fig. 5j). In addition, given that entry into torpor requires hours of fasting, and involves many neuronal populations in which the FOS transcription factor is induced, one possibility is that activity-dependent gene transcription has a mechanistic role in establishing a state that is permissive for torpor entry.

Because torpor is a dynamic and complex behaviour that involves profound changes in body temperature, metabolic rate, locomotion, perception, breathing and heart rate[7,10], the engagement of other neuronal populations and brain regions—including additional torpor-associated neurons identified here by the FosTRAP approach and by snRNA-seq—is likely to be involved in orchestrating the full program of natural torpor entry, maintenance and arousal. The elucidation of torpor-regulating neuronal circuitry will enable an investigation of the mechanisms by which this circuit inhibits, circumvents or inverts normal cold defensive thermoregulatory processes[1,2,50]. This should provide insight into why only certain mammalian species have the ability to enter torpor, and whether such a hypometabolic state could be induced in species that typically do not enter torpor. For example, although rats and humans do not naturally enter torpor, a study has recapitulated attributes of torpor in rats[39], suggesting the possibility of inducing a similar state in humans. Future investigations should deliver further advances through the study and manipulation of these ancient adaptations of homeotherm biology.

Online content

Any methods, additional references, Nature Research reporting summaries, source data, extended data, supplementary information, acknowledgements, peer review information; details of author contributions and competing interests; and statements of data and code availability are available at https://doi.org/10.1038/s41586-020-2387-5.

1. Tan, C. L. & Knight, Z. A. Regulation of body temperature by the nervous system. *Neuron* **98**, 31–48 (2018).
2. Morrison, S. F. & Nakamura, K. Central mechanisms for thermoregulation. *Annu. Rev. Physiol.* **81**, 285–308 (2019).
3. Heller, H. C. & Hammel, H. T. CNS control of body temperature during hibernation. *Comp. Biochem. Physiol. A* **41**, 349–359 (1972).
4. Sunagawa, G. A. & Takahashi, M. Hypometabolism during daily torpor in mice is dominated by reduction in the sensitivity of the thermoregulatory system. *Sci. Rep.* **6**, 37011 (2016).
5. Geiser, F. Metabolic rate and body temperature reduction during hibernation and daily torpor. *Annu. Rev. Physiol.* **66**, 239–274 (2004).
6. Morton, S. R. Torpor and nest-sharing in free-living S *minthopsis crassicaudata* (Marsupialia) and *Mus musculus* (Rodentia). *J. Mamm.* **59**, 569–575 (1978).
7. Heldmaier, G., Ortmann, S. & Elvert, R. Natural hypometabolism during hibernation and daily torpor in mammals. *Respir. Physiol. Neurobiol.* **141**, 317–329 (2004).
8. Hoffstaetter, L. J., Bagriantsev, S. N. & Gracheva, E. O. TRPs et al.: a molecular toolkit for thermosensory adaptations. *Pflugers Arch.* **470**, 745–759 (2018).
9. Barnes, B. M. Freeze avoidance in a mammal: body temperatures below 0 °C in an Arctic hibernator. *Science* **244**, 1593–1595 (1989).
10. Swoap, S. J. & Gutilla, M. J. Cardiovascular changes during daily torpor in the laboratory mouse. *Am. J. Physiol. Regul. Integr. Comp. Physiol.* **297**, R769–R774 (2009).
11. Revel, F. G. et al. The circadian clock stops ticking during deep hibernation in the European hamster. *Proc. Natl Acad. Sci. USA* **104**, 13816–13820 (2007).
12. Teague, R. S. & Ranson, S. W. The role of the anterior hypothalamus in temperature regulation. *Am. J. Physiol.* **117**, 562–570 (1936).
13. Zaretskaia, M. V., Zaretsky, D. V., Shekhar, A. & DiMicco, J. A. Chemical stimulation of the dorsomedial hypothalamus evokes non-shivering thermogenesis in anesthetized rats. *Brain Res.* **928**, 113–125 (2002).
14. Schneeberger, M. et al. Regulation of energy expenditure by brainstem GABA neurons. *Cell* **178**, 672–685 (2019).
15. Boulant, J. A. & Hardy, J. D. The effect of spinal and skin temperatures on the firing rate and thermosensitivity of preoptic neurones. *J. Physiol. (Lond.)* **240**, 639–660 (1974).
16. Tan, C. L. et al. Warm-sensitive neurons that control body temperature. *Cell* **167**, 47–59 (2016).
17. Yu, S. et al. Glutamatergic preoptic area neurons that express leptin receptors drive temperature-dependent body weight homeostasis. *J. Neurosci.* **36**, 5034–5046 (2016).
18. Harding, E. C. et al. A neuronal hub binding sleep initiation and body cooling in response to a warm external stimulus. *Curr. Biol.* **28**, 2263–2273 (2018).
19. Nakayama, T., Eisenman, J. S. & Hardy, J. D. Single unit activity of anterior hypothalamus during local heating. *Science* **134**, 560–561 (1961).
20. Wang, T. A. et al. Thermoregulation via temperature-dependent PGD_2 production in mouse preoptic area. *Neuron* **103**, 309–322 (2019).
21. Feketa, V. V., Nikolaev, Y. A., Merriman, D. K., Bagriantsev, S. N. & Gracheva, E. O. CNGA3 acts as a cold sensor in hypothalamic neurons. *eLife* **9**, e55370 (2020).
22. Herrington, L. P. The heat regulation of small laboratory animals at various environmental temperatures. *Am. J. Physiol.* **129**, 123–139 (1940).
23. Reitman, M. L. Of mice and men – environmental temperature, body temperature, and treatment of obesity. *FEBS Lett.* **592**, 2098–2107 (2018).
24. Padilla, S. L. et al. Agouti-related peptide neural circuits mediate adaptive behaviors in the starved state. *Nat. Neurosci.* **19**, 734–741 (2016).
25. Jensen, T. L., Kiersgaard, M. K., Sørensen, D. B. & Mikkelsen, L. F. Fasting of mice: a review. *Lab. Anim.* **47**, 225–240 (2013).
26. Hitrec, T. et al. Neural control of fasting-induced torpor in mice. *Sci. Rep.* **9**, 15462 (2019).
27. Gavrilova, O. et al. Torpor in mice is induced by both leptin-dependent and -independent mechanisms. *Proc. Natl Acad. Sci. USA* **96**, 14623–14628 (1999).
28. van der Vinne, V., Bingaman, M. J., Weaver, D. R. & Swoap, S. J. Clocks and meals keep mice from being cool. *J. Exp. Biol.* **221**, jeb179812 (2018).
29. Himms-Hagen, J. Food restriction increases torpor and improves brown adipose tissue thermogenesis in ob/ob mice. *Am. J. Physiol. Endocrinol. Metab.* **248**, E531–E539 (1985).
30. Swoap, S. J., Gutilla, M. J., Liles, L. C., Smith, R. O. & Weinshenker, D. The full expression of fasting-induced torpor requires β3-adrenergic receptor signaling. *J. Neurosci.* **26**, 241–245 (2006).
31. Greenberg, M. E., Ziff, E. B. & Greene, L. A. Stimulation of neuronal acetylcholine receptors induces rapid gene transcription. *Science* **234**, 80–83 (1986).
32. *Allen Mouse Brain Atlas* (Allen Institute for Brain Science, 2019); http://mouse.brain-map.org
33. Wu, Q. et al. The temporal pattern of cfos activation in hypothalamic, cortical, and brainstem nuclei in response to fasting and refeeding in male mice. *Endocrinology* **155**, 840–853 (2014).
34. Andermann, M. L. & Lowell, B. B. Toward a wiring diagram understanding of appetite control. *Neuron* **95**, 757–778 (2017).
35. Nectow, A. R. et al. Identification of a brainstem circuit controlling feeding. *Cell* **170**, 429–442 (2017).
36. Allen, W. E. et al. Thirst-associated preoptic neurons encode an aversive motivational drive. *Science* **357**, 1149–1155 (2017).
37. Zhu, H. et al. Cre-dependent DREADD (Designer Receptors Exclusively Activated by Designer Drugs) mice. *Genesis* **54**, 439–446 (2016).
38. Geiser, F., Currie, S. E., O'Shea, K. A. & Hiebert, S. M. Torpor and hypothermia: reversed hysteresis of metabolic rate and body temperature. *Am. J. Physiol. Regul. Integr. Comp. Physiol.* **307**, R1324–R1329 (2014).
39. Tupone, D., Madden, C. J. & Morrison, S. F. Central activation of the A1 adenosine receptor (A1AR) induces a hypothermic, torpor-like state in the rat. *J. Neurosci.* **33**, 14512–14525 (2013).
40. McKinley, M. J. et al. The median preoptic nucleus: front and centre for the regulation of body fluid, sodium, temperature, sleep and cardiovascular homeostasis. *Acta Physiol. (Oxf.)* **214**, 8–32 (2015).
41. Moffitt, J. R. et al. Molecular, spatial, and functional single-cell profiling of the hypothalamic preoptic region. *Science* **362**, eaau5324 (2018).
42. Sherin, J. E., Shiromani, P. J., McCarley, R. W. & Saper, C. B. Activation of ventrolateral preoptic neurons during sleep. *Science* **271**, 216–219 (1996).
43. Chung, S. et al. Identification of preoptic sleep neurons using retrograde labelling and gene profiling. *Nature* **545**, 477–481 (2017).
44. Li, S.-B. & de Lecea, L. The hypocretin (orexin) system: from a neural circuitry perspective. *Neuropharmacology* **167**, 107993 (2020).
45. Habib, N. et al. Massively parallel single-nucleus RNA-seq with DroNc-seq. *Nat. Methods* **14**, 955–958 (2017).
46. Zhao, Z.-D. et al. A hypothalamic circuit that controls body temperature. *Proc. Natl Acad. Sci. USA* **114**, 2042–2047 (2017).
47. Yamamoto, M. et al. Reversible suppression of glutamatergic neurotransmission of cerebellar granule cells in vivo by genetically manipulated expression of tetanus neurotoxin light chain. *J. Neurosci.* **23**, 6759–6767 (2003).
48. Chen, T.-W. et al. Ultrasensitive fluorescent proteins for imaging neuronal activity. *Nature* **499**, 295–300 (2013).
49. Carlin, J. L. et al. Hypothermia in mouse is caused by adenosine A_1 and A_3 receptor agonists and AMP via three distinct mechanisms. *Neuropharmacology* **114**, 101–113 (2017).
50. Tupone, D., Cano, G. & Morrison, S. F. Thermoregulatory inversion: a novel thermoregulatory paradigm. *Am. J. Physiol. Regul. Integr. Comp. Physiol.* **312**, R779–R786 (2017).

Publisher's note Springer Nature remains neutral with regard to jurisdictional claims in published maps and institutional affiliations.

© The Author(s), under exclusive licence to Springer Nature Limited 2020

Methods

Mice

Animal experiments were approved by the National Institutes of Health and Harvard Medical School Institutional Animal Care and Use Committee, following ethical guidelines described in the US National Institutes of Health Guide for the Care and Use of Laboratory Animals. For initial torpor experiments, we used adult (6–10-week-old) C57BL/6J mice (The Jackson Laboratory, Stock 000664). To generate FosTRAP-Gq mice we crossed Fos2A-iCreER (TRAP2) mice (The Jackson Laboratory, Stock 030323) with R26-LSL-Gq-DREADD mice (The Jackson Laboratory, Stock 026220) and used adult (6–18-week-old) male and female F_1 progeny. For viral injections we used Fos2A-iCreER (TRAP2) mice (The Jackson Laboratory, Stock 030323), Adcyap1-2A-Cre mice (The Jackson Laboratory, Stock 030155), Vglut2-ires-Cre mice (The Jackson Laboratory, Stock 028863) and Vgat-ires-Cre mice (The Jackson Laboratory, Stock 028862). All mice were housed at 22 °C under a standard 12 h light/dark cycle.

No statistical methods were used to predetermine the sample size. Mice were randomly assigned to experimental groups before surgery. Where possible, investigators were blinded during analysis.

Telemetric monitoring of core body temperature and gross motor activity

Mice with genotypes of interest were singly housed and implanted abdominally with telemetric temperature and activity probes (Starr Life Science VV-EMITT-G2). After at least four days of recovery, mice were recorded in standard cages placed onto a radiofrequency receiver platform (Starr Life Science ER4000). Core body temperature and gross motor activity were logged every 60 s.

Measurements of oxygen consumption

Oxygen consumption was measured using the Columbus Instruments Comprehensive Lab Animal Monitoring System (CLAMS) at the Brigham and Women's Hospital or the Beth Israel Deaconess Medical Center Metabolic Core. Individual mice were placed into metabolic cages enabling the measurement of oxygen consumption (recorded as VO_2, the volume of O_2 consumed per unit time). The CLAMS system is compatible with simultaneous measurements of core body temperature and gross motor activity using the implanted telemetric probes.

Torpor induction

Adult (6–18-week-old) mice were singly housed before the induction of torpor. Each mouse was moved to a new individual cage containing water and nesting material but devoid of bedding and food at the beginning of the dark cycle. Initial bouts of torpor were observed after approximately 8 h of fasting. Mice were returned to their standard cages containing food 24 h after the start of the fast. The ambient temperature of the facility was maintained at around 22 °C.

TRAPing

To label neurons that are active during torpor, we used mice harbouring a tamoxifen-dependent form of Cre recombinase (CreERT2) driven from the *Fos* locus ($Fos^{2A\text{-}iCreERT2}$, FosTRAP[36]). When these mice are fasted to enter torpor, the neurons that are active induce FOS and CreERT2. When these mice are exposed to 4-OHT (Sigma-Aldrich, H6278), the CreERT2 will translocate to the nucleus. Once translocated, CreERT2 can recombine the genomically encoded Cre-dependent R26-LSL-Gq-DREADD allele or the virally introduced Cre-dependent AAV-DIO-Gq-DREADD–mCherry construct selectively in the FOS-expressing cells. This recombination leads to the persistent expression of Gq-DREADD and allows for the activation of these specific 'TRAPed' neurons at a later time by the administration of CNO[51].

4-OHT solution was prepared by initially dissolving 10 mg of 4-OHT in 500 µl of 100% ethanol, then adding 450 µl of a 1:4 mixture of castor oil:sunflower oil and vortexing. The ethanol was removed via vacuum centrifugation, and the remaining 4-OHT solution was diluted with the same 1:4 mixture of castor oil:sunflower oil to a final concentration of approximately 6.25 mg ml^{-1}. For TRAPing, each mouse was injected intraperitoneally with 50 mg kg^{-1} of 4-OHT during torpor entry.

CNO solution was prepared by initially dissolving CNO hydrochloride (Sigma-Aldrich, SML2304) in H_2O to a stock solution of 100 mM. The stock solution was diluted with PBS to a final concentration of 0.6 mM, and approximately 250 µl was injected intraperitoneally per mouse for a final injection concentration of 2 mg kg^{-1}.

Immunofluorescent staining

Mice were euthanized by transcardial perfusion of 10 ml PBS followed by 10 ml of 4% paraformaldehyde (PFA). Brains were extracted, post-fixed overnight with 4% PFA at 4 °C and then embedded in PBS with 3% agarose. Brains were sliced on a vibratome (Leica VT1000S) into 50-µm coronal sections. Coronal sections were washed three times with PBS containing 0.3% TritonX-100 (PBST) and blocked for 1 h at room temperature with PBST containing 5% donkey serum (blocking buffer). Sections were incubated overnight at 4 °C with primary antibodies diluted in blocking buffer, washed again three times with PBST, and incubated for 1 h at room temperature with secondary antibodies diluted in blocking buffer. After washing twice in PBST and once in PBS, samples were mounted onto SuperFrost Plus glass slides (VWR) using DAPI Fluoromount-G.

Detection of FOS^+ and Gq-DREADD-HA^+ cells

Tissues were processed as indicated in the section 'Immunofluorescent staining' using the following reagents: primary antibodies: rabbit anti-FOS antibody 1:2,000 (Cedarlane, 226003(SY)) and rabbit anti-haemagglutinin (HA) antibody 1:1,000 (Cell Signaling Technology, 3724S). Secondary antibody: 1:500 donkey anti-rabbit 647 secondary antibody (Life Technologies, A31573).

Sections were imaged on an Olympus BX61VS microscope using a UPlanSApo 10 × 0.4 objective (Harvard NeuroDiscovery Center).

Image registration to the Allen Brain Atlas and analysis

Imaged immunofluorescent brain slices were converted to TIF format and organized in sequential anterior to posterior order. To quantify the average Gq-DREADD-HA signal and count FOS^+ cells over different brain regions, the brain slices were registered with the Allen Brain Atlas[32] as described previously[52–55], with some custom modifications. There are three main parts to the pipeline: pre-processing, stack registration and plane alignment. The pre-processing stage includes downsizing image files, using a previously trained machine-learning algorithm to compute the brain slice borders, generating a mask and edge map, and detecting puncta if necessary. The stack-registration stage aligns the dataset with itself using the vertical line of symmetry as a guide. In the plane-assignment stage, each internally registered brain slice is paired to the Allen Brain Atlas using an estimate of the bregma value and a method similar to sequence alignment using dynamic programming. After pairwise registration to the Allen Brain Atlas, experimental brain slices are further adjusted using local nonlinear deformations to maximize the fit between the experimental image and the image from the Allen Brain Atlas. Then, the signal intensity and the number of spots are quantified for each brain region defined by the Allen Brain Atlas. Finally, the volume of each brain region is calculated so that the signal density (signal intensity divided by volume) and density of spots (number of spots divided by volume) could be determined.

Several parameters in the pipeline were adjusted to optimally process our experimental brain slices. For both FOS and Gq-DREADD-HA signal quantification, a boundary erosion with radius 1 (after downsizing) was implemented to exclude quantification at the edge of the brain slices, where inaccuracies during the experimental preparation may occur. Estimated bregma values for the most anterior and posterior

brain slices were also adjusted on the basis of each sample. To detect individual FOS^+ nuclei via Laplacian of Gaussian filtering of the image, we found and distinguished the local maxima that are FOS puncta from local maxima in the background. The distribution of local maxima in the background was computed, and the threshold distance to background distribution was set to 7 to indicate that only spots 7 standard deviations away from the mean of the background distribution were selected. For selected spots (putative FOS^+ nuclei), their correlation with the ideal circular spot was measured, and any spot with a correlation below 0.5 was eliminated. These parameters were ignored when the FosTRAP-Gq-HA brain signal was quantified, as the haemagglutinin signal was not nuclear and was instead distributed across the cell body and neuronal processes, and thus could not be modelled and quantified as a circular spot.

Viral constructs

AAV8-hSyn-DIO-Gq–mCherry (Addgene, 44361-AAV8) and AAV1-Syn-Flex-GCaMP6s-WPRE-SV40 (Addgene, 100845-AAV1) were obtained from Addgene. AAV2/1-hSyn-Flex-TeLC-eYFP[56] was prepared through Boston Children's Hospital Viral Core. All viruses were diluted with PBS to a final concentration between 5×10^{12} and 1×10^{13} genome copies per ml before stereotaxic delivery into the mouse brain.

Stereotactic viral injection and photometry fibre implantation

For injections, mice were anaesthetized with 3% isoflurane and placed in a stereotaxic head frame (Kopf Instrument, model 1900). Coordinates AP +0.4 mm, ML ±0.5 mm, DV −5.1 mm relative to bregma, were used for all avMLPA injection. Unless otherwise specified, all experiments were carried out with bilateral injections. An air-based injection system built with Digital Manometer (Grainger, 9LHH8) was used to infuse the virus. The virus was infused at approximately 100 nl min^{-1}, and the needle was kept at the injection site for 10 min before withdrawing. For chemogenetic stimulation, about 25–100 nl of AAV8-hSyn-DIO-Gq–mCherry was delivered into the region of interest. For fibre photometry recordings, 200 nl of a mixture (1:1 ratio) of AAV8-hSyn-DIO-Gq–mCherry and AAV1-Syn-Flex-GCaMP6s-WPRE-SV40 was delivered into the region of interest, either unilaterally or bilaterally. For fibre photometry recording, Mono Fibre-optic cannulas (Doric, MFC_200/230-0.37_###_MF1.25_FLT) were implanted 200 µm above the injection site. The fibre was fixed to the skull with Loctite 454 Instant Adhesive and further covered by dental cement to ensure the stability of the implant.

Mapping of virally injected hypothalamic nuclei and correlation with chemogenetically induced changes in core body temperature

Viral injection, sample preparation and imaging. To minimize initial differences in body weight between mice, which might influence the effects on core body temperature and confound our screen across brain regions, we used a cohort of fifty-four 6–10-week-old female FosTRAP mice. Mice were bilaterally injected with AAV8-hSyn-DIO-Gq–mCherry, allowed to recover for 4–10 days and then fasted and injected with 4-OHT during torpor to TRAP active neurons. Subsequently (3–14 days later), mice were administered CNO to stimulate fast-TRAPed neurons within the virally injected regions and their core body temperature and activity were recorded. Given that different mice were injected in different hypothalamic areas and that no two injections will be identical due to the subtle variabilities in the injection site and viral spread, all mice were euthanized to map post hoc the exact brain regions that were transduced and contained TRAPed neurons. Mice were euthanized by transcardial perfusion of 10 ml PBS followed by 10 ml of 4% PFA. Brains were extracted, post-fixed overnight with 4% PFA at 4 °C and then embedded in PBS with 3% agarose. Brains were sliced on a vibratome (Leica VT1000S) into 50 µm coronal sections, mounted onto glass slides and imaged on an Olympus BX61VS microscope using a UPlanSApo 10 × 0.4 objective (Harvard NeuroDiscovery Center). The expression of AAV-DIO-Gq-DREADD–mCherry was detected by its endogenous fluorescence.

Image analysis. Viral mCherry expression was quantified across 277 hypothalamic regions, noting semiquantitatively for each region and each hemisphere whether the viral expression was 0 (none), 1 (minimal), 2 (partial) or 3 (total; Fig. 2b, Supplementary Table 3). The analysis was performed blinded to the effect on core body temperature that was previously observed in each mouse.

Correlation with changes in core body temperature. To assign a single numeric value for each hypothalamic region in each mouse, we added the semiquantitative transduction values from the two hemispheres. For correlation analysis, we analysed 226 of the 277 brain regions that were transduced in at least three mice. For each region independently, we determined the Pearson correlation across all mice between the viral expression in that region and the decrease in core body temperature that was observed. FDR-corrected q values are shown in Extended Data Fig. 2a–c. For each region independently, we also calculated the average (across mice) minimum temperature that was observed after the chemogenetic stimulation of all mice in which the region was hit (viral expression > 0) and all mice in which the regions were missed (viral expression = 0). Values are plotted in Extended Data Fig. 2a–c.

Nuclear isolation for snRNA-seq

Mice were anaesthetized with 3% isoflurane and transcardially perfused with cold choline dissection media. The brains were extracted and sectioned into 300-µm coronal sections. Sections containing the MPA were microdissected to isolate the avMLPA.

Single-nuclei suspensions for droplet-based snRNA-seq[57–59] were generated as described previously[60], with minor modifications. The avMLPA was dissected and placed into a Dounce with homogenization buffer (0.25 M sucrose, 25 mM KCl, 5 mM $MgCl_2$, 20 mM Tricine-KOH, pH 7.8, 1 mM DTT, 0.15 mM spermine, 0.5 mM spermidine, protease inhibitors). The sample was homogenized using a tight pestle with 10 strokes. IGEPAL solution (5%, Sigma) was added to a final concentration of 0.32%, and 5 additional strokes were performed. The homogenate was filtered through a 40-µm filter, and OptiPrep (Sigma) was added to a final concentration of 25% iodixanol. The sample was layered onto an iodixanol gradient and centrifuged at 10,000g for 18 min as previously described[59,60]. Nuclei were collected between the 30% and 40% iodixanol layers and diluted to 80,000-100,000 nuclei per ml for encapsulation. All buffers contained 0.15% RNasin Plus RNase Inhibitor (Promega) and 0.04% BSA.

avMLPA snRNA-seq

snRNA-seq library preparation and sequencing. Single nuclei were captured and barcoded for whole-transcriptome libraries using the 10X Genomics Chromium v2 platform according to the manufacturer's recommendations, collecting one library of approximately 10,000 nuclei from each of the 5 mice. In brief, single nuclei along with single primer-carrying hydrogels were captured into droplets using a microfluidic device. Each hydrogel carried oligodT primers with a unique cell barcode. Nuclei were lysed and the cell-barcode-containing primers released from the hydrogel, initiating reverse transcription and barcoding of all cDNA in each droplet. Next, the emulsions were broken and cDNA across approximately 10,000 nuclei were pooled into the same library. The cDNA was amplified, fragmented and adapters were added for sequencing on a Nextseq 500 benchtop DNA sequencer (Illumina).

For enrichment of virally derived transcripts, a fraction (1 µl) of the non-fragmented cDNA was PCR-amplified. The forward primer (5′-GCATGGACGAGCTGTACA) was designed to anneal to the sequence uniquely present at the 3′ terminus of mCherry. The reverse primer (5′-CTACACGACGCTCTTCCG) was designed to anneal to the R1

sequence, uniquely present at the 5′ terminus, to the 10X barcode and unique molecular identifier (UMI) sequence that were introduced during the reverse transcription. The result of the PCR is preferential amplification of the viral-derived transcripts, while simultaneously retaining the cell-barcode sequence necessary to assign each viral transcript to a particular cell or nucleus. After PCR amplification (18 cycles, Hot Start High-Fidelity Q5 polymerase, NEB, M0494S), the product was purified using 0.6X SPRI select reagent (Thermo Fisher Scientific, NC0406406) and 1 µl of the 50 µl eluent was used in a second PCR reaction. The forward primer for the second PCR (5′-GTGACTGGAGTTCAGACGTG TGCTCTTCCGATCTgtaaggcgcgccataac) was designed to anneal to the sequence uniquely present between the *mCherry* and *loxP* sites of the AAV-DIO-Gq-DREADD–mCherry vector. In addition, this primer introduced the R2 sequence necessary for later library amplification. The reverse primer (5′-CTACACGACGCTCTTCCG) was the same as in the first PCR reaction. The result of the PCR is again preferential amplification of the viral-derived transcripts, while simultaneously retaining the cell-barcode sequence necessary to assign each viral transcript to a particular cell or nucleus. After PCR amplification (18 cycles, Hot Start High-Fidelity Q5 polymerase, NEB, M0494S), all the libraries were indexed according to the 10X protocol, pooled, and sequenced on a Nextseq 500 benchtop DNA sequencer (Illumina).

snRNA-seq sample mapping and viral barcode deconvolution by cell. The 10X Genomics package cellranger 3.1.0 was used to map transcripts to the mm10 reference mouse genome. Because snRNA-seq captures unspliced pre-mRNA as well as mature mRNA, we created a custom 'pre-mRNA' gene annotation file, in which all features are recoded as exons, enabling us to map unspliced reads to these artificial exons and to assign them to the corresponding genes. Feature barcoding with custom features was used to assign viral mRNA reads to cells and distinguish between the transcript sequence from the initial AAV-DIO-Gq-DREADD–mCherry vector and the transcript sequence produced by the Cre-recombined vector in TRAPed neurons.

Doublet removal, embedding and identification of main cell classes. Microfluidic encapsulation of nuclei results in some droplets containing more than one nucleus. During reverse transcription, transcripts from co-encapsulated nuclei would be labelled with the same cell barcode, effectively creating a hybrid cell or a 'doublet'. To detect and remove predicted doublets using bioinformatics, each of the five libraries were independently processed using the *scrublet* package[61] with the following commands:

scrub = scr.Scrublet(counts_matrix, expected_doublet_rate = 0.10)

doublet_scores, predicted_doublets = scrub.scrub_doublets(min_counts = 2, min_cells = 3, min_gene_variability_pctl = 85, n_prin_comps = 30).

Doublet-removal eliminated 2,037 cells, leaving 44,669 nuclei across five libraries for further processing. We recovered an average of 2,083 unique non-viral transcripts per nucleus, representing 1,286 unique genes (Extended Data Fig. 3). Data from all nuclei were analysed simultaneously and virally derived sequences were removed for the purposes of embedding, clustering and cell-type identification. The R software package Seurat 3.1[58,62] was used to assign cells to clusters. Any genes that were expressed in fewer than three cells were removed from the analysis. Data was normalized with the number of transcripts per cell and the per cent transcripts derived from the mitochondrial genes regressed using the SCTransform function with default parameters. Initially, the 3,000 most variable genes were identified.

Tissue dissociation has been shown to increase the expression of mitochondrial RNAs, ribosomal-protein RNAs, and immediate–early genes[63–65]. To minimize the influence of these tissue-processing-induced genes on the identification and molecular characterization of avMLPA cells, we removed from the initial list of 3,000 most variable genes any genes that were identified as mitochondrial, ribosomal-protein-encoding or were the immediate–early genes *Fos*, *Fosb*, *Fosl1*, *Fosl2*, *Egr1* and *Npas4*. To further diminish any potential effects of tissue-dissociation-induced expression changes on clustering, we identified and removed from the list of variable genes any genes for which their expression across all cells correlated with any mitochondrial, ribosomal-protein-encoding or immediate–early genes listed above[41,58,66] (Pearson correlation coefficient greater than 0.2 or smaller than −0.2). The final list contained 2,827 variable genes. Next, principal component analysis (PCA) was carried out using the *RunPCA()* function. The *FindNeighbours()* function, using the top 30 principal components (PCs) and the *FindClusters()*, was used to identify the initial 34 clusters. Clusters that were disproportionately derived from a single sample were removed, leaving 39,562 cells. On the basis of the expression of known marker genes, we merged clusters that represented the same cell type. Our final list of cell types was: glutamatergic neurons (Glut), GABAergic neurons (GABA), cholinergic neurons (Chol), astrocytes (Astro), endothelial cells (Endo), microglia (Micro), oligodendrocytes (Oligo) and oligodendrocyte precursor cells (OPCs) (Fig. 3b, c).

Identification of neuronal subtypes. Cells classified as neurons (n = 28,103 cells) were additionally processed to identify neuronal subtypes in the avMLPA. The same Seurat 3.1.0 pipeline was used as described in the section 'Doublet removal, embedding and identification of main cell classes'. Clustering identified 24 GABAergic, 8 glutamatergic, 3 hybrid and 1 cholinergic neuronal cell type (Fig. 3d). The function *FindAllMarkers(seurat_mat, only.pos = F, min.pct = 0.1, thresh.use = 0.25)* uses a Bonferroni-corrected (across 23,967 genes in the dataset) two-tailed Mann–Whitney *U*-test to perform differential gene expression analysis and identify markers of each cell type. The top five markers based on fold enrichment are plotted in Extended Data Fig. 4. The top 20 markers are displayed in Supplementary Table 4. Cross-referencing these markers with previously described markers for cell types in the MPA[41] led to the annotation of the 36 neuronal cell types indicated in Fig. 3e.

Hierarchical tree construction. Neuronal cell types were clustered on the basis of average gene expression across all 2,954 variable genes. A distance matrix was then calculated in Euclidean space and hierarchical clustering was carried out using the function *hclust* and the *ward.D* method.

Identification of TRAPed neurons in snRNA-seq data. Feature barcoding with custom features identified for each nucleus the number of viral mRNA reads that were derived from the non-recombined AAV-DIO-Gq-DREADD–mCherry vector and the number of viral mRNA reads from the Cre-recombined AAV-DIO-Gq-DREADD–mCherry vector (Extended Data Fig. 5a). Neuronal nuclei or cells containing three or more virally derived transcripts (17,424) were considered transduced by the AAV. Among them, 343 neuronal nuclei or cells contained three or more virally derived transcripts for which the mRNA sequence indicated that the vector had been recombined by Cre, suggesting that these cells were previously TRAPed and now express the Gq-DREADD–mCherry protein.

Differential gene expression between TRAPed and non-TRAPed *Adcyap1*$^+$ neurons. Differential gene expression analysis was carried out between TRAPed (n = 139 cells) and non-TRAPed (n = 5,848 cells) *Adcyap1*+ neurons in the snRNA-seq dataset. The FindMarkers(PACAP.cells, ident.1 = "TRAP", ident.2 = "Non-TRAP", verbose = FALSE) function in the R software package Seurat 3.1 was used to perform a Bonferroni-corrected (across 23,967 genes in the data set) two-tailed Mann–Whitney *U*-test and identify differentially expressed genes.

Combined fluorescence in situ hybridization and immunofluorescence

Fluorescence in situ hybridization. Mice were euthanized by transcardial perfusion of 10 ml PBS followed by 10 ml of 4% PFA. Brains were

extracted, post-fixed overnight with 4% PFA at 4 °C and then incubated in PBS with 30% sucrose for 48 h at 4 °C for cryoprotection. Brains were embedded in tissue freezing medium and frozen in 2-methylbutane that had been cooled by liquid nitrogen. Brains were sliced on a cryostat (Leica CM1950) into 20-µm sections, adhered to SuperFrost Plus slides (VWR) and immediately stored at −80 °C until use. Samples were processed according to the ACD RNAscope Fluorescent Multiplex Assay manual with the following modifications: 500 ml of 1x Antigen retrieval solution was heated to 99–100 °C and maintained at a uniform boil. The slides of fixed frozen brain slices, stored at −80 °C, were immediately placed into a slide rack and slowly submerged into the boiling 1x Antigen retrieval solution for 5 min. Immediately afterwards, the slides were washed 3–5 times by moving the slide rack up and down in Milli-Q H_2O and washed again in 100% EtOH at room temperature. A hydrophobic barrier was drawn around each slice and it was allowed to dry for 1 min at room temperature. From this point on, the procedure followed the standard in situ hybridization protocol for RNAscope Fluorescent Multiplex Assay.

Immunofluorescence. Slides were washed twice for 2 min in PBST (PBS + 0.01% Tween) and blocked by incubation with 1% BSA and 10% donkey serum in PBST for 30 min room temperature. They were then incubated with primary antibody diluted in PBS + 1% BSA overnight at 4 °C and washed three times for 5 min with PBST. Slides were subsequently incubated with secondary antibody diluted in PBS + 1% BSA for 1 h at room temperature, washed with PBST three times for 2 min at room temperature, stained with DAPI (RNAscope), and finally mounted with ProLong Gold antifade reagent.

Determining markers of torpor-TRAPed avMLPA neurons

Brains were processed as indicated in the section 'Combined fluorescence in situ hybridization and immunofluorescence' using the following reagents: for the detection of mCherry$^+$ cells, 1:300 rabbit anti-mCherry (Abcam, ab167453) was used as the primary antibody and 1:500 donkey anti-rabbit 568 (Life Technologies, AB_2534017) as the secondary antibody.

Sample imaging. Sections containing avMLPA were imaged on a Leica SPE confocal microscope using an ACS APO 20×/0.60 IMM CORR objective (Harvard NeuroDiscovery Center). Tiled MPA areas were imaged with a single optical section to avoid counting the same cell across multiple optical sections. Channels were imaged sequentially to avoid any optical crosstalk.

Image analysis. To determine the fraction of TRAPed mCherry$^+$ cells that express each marker gene, in each image mCherry$^+$ cells were manually marked while staying blinded to the in situ hybridization signals (*Adcyap1*, *Vglut2*, *Vgat*). Because mCherry was fused to the Gq-DREADD and thus largely membrane-bound, we reasoned that manually marking mCherry$^+$ cells would provide a more accurate measurement compared to semi-automated algorithms that are optimized for a more focal (nuclear or cytoplasmic) signal. After the identification of mCherry$^+$ cells, for each cell we evaluated whether it appeared positive for markers detected by in situ hybridization, staying blinded to the identity of the marker that was being evaluated. To determine the fraction of marker$^+$ cells that are mCherry$^+$, we additionally counted the total number of marker$^+$ cells.

Mapping anterograde projections of torpor-TRAPed avMLPA neurons

FosTRAP mice that were injected with AAV8-hSyn-DIO-Gq–mCherry and TRAPed during natural torpor were euthanized 2 months later. Brains were processed as indicated in the section 'Immunofluorescent staining' using the following reagents: primary antibody: 1:300 rabbit anti-mCherry antibody (Abcam, ab167453); secondary antibody: donkey anti-rabbit 647 secondary antibody (Life Technologies, A31573). Sections were imaged on an Olympus BX61VS microscope using a UPlanSApo 10× 0.4 objective (Harvard NeuroDiscovery Center).

Silencing avMLPA neurons

The avMLPA of male and female Adcyap1-2A-Cre and Vglut2-IRES-Cre mice was injected with approximately 100–150 nl AAV-DIO-Gq-DREADD–mCherry and AAV-Flex-TeLC–eYFP (1:1 ratio). Control mice were injected with AAV-DIO-Gq-DREADD–mCherry and/or AAV-Flex-GCaMP6s. After 5–14 days of recovery from surgery, mice were fasted to induce torpor and their core body temperature was monitored. The minimum core body temperature is shown in Fig. 4d–f, Extended Data Fig. 8j–m. To analyse the kinetics of torpor, we calculated the time it took each mouse to reach minimum body temperature, requiring that the minimum body temperature is at least as low as the 10th percentile of the body temperature observed in control fed mice (33.2 °C). To avoid counting smaller oscillations in body temperature in this analysis, we classified the mice as not having entered torpor if the body temperature of a fasted mouse did not decrease below this threshold. In this case, we assigned the time it took to reach the minimum body temperature ('Time to Min. T_b') to be 24 h, indicating that the mouse did not decrease its body temperature below this required threshold during the 24-h recording.

Identification of *Adcyap1*$^+$ cells that express TeLC–eYFP

Sample preparation. TeLC-silenced Adcyap1-2A-Cre mice were euthanized and the brains were processed as indicated in section 'Combined fluorescence in situ hybridization and immunofluorescence' using the following reagents: for the detection of TeLC–eYFP$^+$ cells 1:1,000 chicken anti-GFP antibody (Abcam, ab13970) was used as the primary antibody and 1:500 donkey anti-chicken 488 antibody (Jackson ImmunoResearch Laboratories, 703-545-155) as the secondary antibody.

Sample imaging. Sections containing avMLPA were imaged on a Leica SPE confocal microscope using an ACS APO 20×/0.60 IMM CORR objective (Harvard NeuroDiscovery Center). Tiled MPA areas were imaged with a single optical section to avoid counting the same cell across multiple optical sections. Channels were imaged sequentially to avoid any optical crosstalk.

Image analysis. To determine the fraction of ISH *Adcyap1*$^+$ cells that are co-positive for eYFP, *Adcyap1*$^+$ cells in each image were manually marked while staying blinded to the eYFP$^+$ cells. After the identification of *Adcyap1*$^+$ cells, each cell was evaluated for whether it appeared positive for eYFP.

Fibre photometry

Set-up. A three-channel multi-fibre photometry system (Neurophotometrics Ltd) was used for these experiments. In brief, light from three LEDs of different wavelengths (470 nm and 560 nm in phase, and 415 nm out of phase) were bandpass filtered and directed down a fibre-optic patch cord via a 20× objective. This was coupled to a fibre-optic cannula implanted in the mouse. Fluorescence emission from GCaMP6s and mCherry was collected through the same cannula and patch cord, split by a 532-nm longpass dichroic, bandpass filtered, and focused onto opposite sides of a CMOS camera sensor.

Data were acquired and quantified using the open-source software Bonsai[67] by drawing a region of interest around the two images (green and red) of the patch cord and calculating the mean pixel value. To perform longitudinal fibre photometry recordings, the duty cycle of the excitation light was decreased to 10% (interleaved 470 nm + 560 nm / 415 nm with 25 ms period at 4 Hz). LED light was delivered at the minimum power and resulted in about 15 µW of 470 nm light and 25 µW of total light at the tip of the patch cord. A pigtailed fibre-optic rotary joint (Doric FRJ_1x1_PT_200/220/LWMJ-0.37_1.0_FCM_0.15_FCM) was connected to the patch cord (Doric MFP_200/220/900-0.37_#.#_FC_MF1.25) to eliminate bending and coiling of the patch cord.

Fasting and CHA-administration photometry session. Mice were placed in custom-built cages to allow free movement during the entire recording session in the dark. The cages were placed onto radiofrequency receiver platforms (Starr Life Science ER4000). Core body temperature and gross motor activity were logged every 10 s. For fasting-induced torpor sessions, water and nesting material only were provided. The fasting was initiated at the beginning of the dark cycle, while the recordings were started up to several hours after the onset of fasting. For CHA-administration sessions, mice were given access to excess food so as to be maintained in a fed state. CHA (0.2 mg kg^{-1}) was administered via intraperitoneal injection without pausing the recordings.

Analysis of torpor entry, maintenance and arousal for fibre photometry. Within each recording session, a temperature threshold was determined under which the mouse was considered to be in torpor. This threshold was set as 2 °C below the top 95% percentile of the temperatures recorded during the entire session (35.6 ± 0.2 °C, mean ± s.e.m.). Any time the mouse was in torpor (as determined by low core body temperature) and the core body temperature was decreasing by more than 0.05 °C min^{-1} the mouse was considered to be entering torpor (Fig. 4i). Anytime the mouse was in torpor (as determined by low core body temperature) and its core body temperature was increasing by more than 0.1 °C min^{-1} the mouse was considered to be arousing from torpor (Fig. 4j).

Analysis of fibre-photometry data. Custom-written MATLAB software was used to analyse photometry data. Background signal measurement (mean signal with excitation lights off) was first subtracted from all signals. To correct for photobleaching and heat-mediated LED decay, the isosbestic signal was fit with a biexponential that was then linearly scaled to the calcium-dependent fluorescence signal F. To calculate dF/F, we divided the signal by this scaled fit. A three-minute sliding window was applied to calculate the local baseline (10th percentile value) and standard deviation of the dF/F values (Extended Data Fig. 9d). Peaks were chosen on the basis of the prominence (top 1%) of all peaks identified with MATLAB *findpeaks* function. The body temperature data set was linearly interpolated, such that the number of samples was equal to the number of photometry data points.

To plot the distribution of the baseline, peak frequency and standard deviation across non-torpor and different stages of torpor, the entire recording was separated into tiled 3-min periods. For each period the average was calculated, and all the 3-min time periods that overlap with each stage of torpor (torpor entry, torpor, torpor arousal) or non-torpor were plotted as a box plot (mean ± s.e.m., Fig. 4m, n, Extended Data Fig. 9e–g).

Temperature challenge. The temperature challenge was set up and performed similarly to that described previously[16]. Food was provided to the mice in the chamber. The raw calcium-dependent GCaMP6s fluorescence signal was smoothed over a 5-element moving average window, and the baseline F was defined as the average fluorescence of a 10-min window at 25 °C before the first ramp of temperature. dF/F was calculated by dividing the smoothed calcium-dependent GCaMP6s signal by the baseline signal.

Fibre-photometry model. Because we observed marked, statistically significant changes in neural activity when mice were entering and maintaining torpor compared with non-torpid mice or mice that were arousing from torpor, we investigated whether fibre-photometry data are sufficient to determine when mice were entering and maintaining torpor. We first extracted several features from our photometry data—baseline signal, frequency of large peaks and the standard deviation—and calculated the average value for each of these features across a 3, 10 and 30-min sliding window, resulting in a total of 9 distinct features. Using these 9 data features, we performed unsupervised k-means clustering across each of the recording sessions ($n = 8$). Silhouette scores were used to determine the optimum number of clusters ($n = 2$), suggesting that fibre photometry data during each recording session could be robustly grouped into two clusters. Next, we asked which of the features that were included in the k-means clustering contributed most to these clusters and observed that the standard deviation and the baseline calculated from the 3-min sliding window were the main contributors. We therefore used these two features to cluster our fibre-photometry data and investigate whether the clusters (states) accurately correlate with the behavioural data for when mice are entering or maintaining torpor. To evaluate the specificity and sensitivity of our model, we cross-referenced the states (clusters) generated by features of the neural data to torpid versus non-torpid periods as defined by movement and body temperature. The sensitivity of the model that was based on the photometry data was calculated by dividing the amount of time that the model accurately determined torpor entry and maintenance by the total amount of time that a mouse spent entering or maintaining torpor (Extended Data Fig. 9j, k). The model specificity was calculated by dividing the amount of time that the model accurately determined torpor entry or maintenance by the total amount of time that the model calculated that the mouse would be entering or maintaining torpor (whether it was accurate or not, Extended Data Fig. 9j, k). To investigate what the accuracy of the model would have been by chance, we randomly shuffled the model output for each of the recording sessions and evaluated the sensitivity and specificity of this shuffled model (Extended Data Fig. 9k).

Reporting summary

Further information on research design is available in the Nature Research Reporting Summary linked to this paper.

Data availability

RNA-sequencing data have been deposited in the Gene Expression Omnibus with accession number GSE149344. Additional data supporting the findings of this study are available from the corresponding authors upon reasonable request.

Code availability

Custom code used in this study is available from the corresponding authors upon reasonable request.

51. Alexander, G. M. et al. Remote control of neuronal activity in transgenic mice expressing evolved G protein-coupled receptors. *Neuron* **63**, 27–39 (2009).
52. Cicconet, M. & Hochbaum, D. R. A. Supervised, symmetry-driven, GUI toolkit for mouse brain stack registration and plane assignment. Preprint at https://www.biorxiv.org/content/10.1101/781880v1 (2019).
53. Lein, E. S. et al. Genome-wide atlas of gene expression in the adult mouse brain. *Nature* **445**, 168–176 (2007).
54. Oh, S. W. et al. A mesoscale connectome of the mouse brain. *Nature* **508**, 207–214 (2014).
55. Renier, N. et al. Mapping of brain activity by automated volume analysis of immediate early genes. *Cell* **165**, 1789–1802 (2016).
56. Zhang, Y. et al. Identifying local and descending inputs for primary sensory neurons. *J. Clin. Invest.* **125**, 3782–3794 (2015).
57. Klein, A. M. et al. Droplet barcoding for single-cell transcriptomics applied to embryonic stem cells. *Cell* **161**, 1187–1201 (2015).
58. Macosko, E. Z. et al. Highly parallel genome-wide expression profiling of individual cells using nanoliter droplets. *Cell* **161**, 1202–1214 (2015).
59. Stroud, H. et al. Early-life gene expression in neurons modulates lasting epigenetic states. *Cell* **171**, 1151–1164 (2017).
60. Hrvatin, S. et al. A scalable platform for the development of cell-type-specific viral drivers. *eLife* **8**, e48089 (2019).
61. Wolock, S. L., Lopez, R. & Klein, A. M. Scrublet: computational identification of cell doublets in single-cell transcriptomic data. *Cell Syst.* **8**, 281–291 (2019).
62. Butler, A., Hoffman, P., Smibert, P., Papalexi, E. & Satija, R. Integrating single-cell transcriptomic data across different conditions, technologies, and species. *Nat. Biotechnol.* **36**, 411–420 (2018).

63. Ilicic, T. et al. Classification of low quality cells from single-cell RNA-seq data. *Genome Biol*. **17**, 29 (2016).
64. van den Brink, S. C. et al. Single-cell sequencing reveals dissociation-induced gene expression in tissue subpopulations. *Nat. Methods* **14**, 935–936 (2017).
65. Hrvatin, S. et al. Single-cell analysis of experience-dependent transcriptomic states in the mouse visual cortex. *Nat. Neurosci*. **21**, 120–129 (2018).
66. Buettner, F. et al. Computational analysis of cell-to-cell heterogeneity in single-cell RNA-sequencing data reveals hidden subpopulations of cells. *Nat. Biotechnol*. **33**, 155–160 (2015).
67. Lopes, G. et al. Bonsai: an event-based framework for processing and controlling data streams. *Front. Neuroinform*. **9**, 7 (2015).

Acknowledgements We thank B. Sabatini, M. Andermann, B. Lowell, C. Saper and S. R. Datta for feedback on this work; members of the Sabatini and W. Regehr laboratories for reagents; members of the Greenberg, Sabatini, Andermann, Lowell and Datta laboratories for discussions; and A. Mina for technical assistance. This project relied on the Beth Israel Deaconess Medical Center Metabolic Core for experiments in metabolic cages, Boston Children's Hospital Viral Core for AAV packaging, the Harvard NeuroDiscovery Center Enhanced Neuroimaging Core and the Neurobiology Imaging Facility (NINDS P30 Core Center grant NS072030) for imaging, the Data Analysis Core at Harvard Medical School for help with image analysis, and the Research Instrumentation Core Facility for engineering support. S.S. acknowledges support from a Herchel Smith Fellowship. This work was supported by National Institutes of Health grants R01 NS028829 and BRAIN Initiative grant R01 MH114081 to M.E.G., R01 DK107717 to A.S.B. and the Warren Alpert Distinguished Scholar Award to S.H.

Author contributions S.H. conceived the study and designed, performed and analysed experiments. S.S. designed, performed and analysed experiments. O.F.W., H.Y., A.J.L.-P., E.G.A. and M.E.P. performed and analysed experiments. S.A. advised on and analysed fibre photometry experiments. M.C. wrote the code to register and analyse images of brain sections. A.S.B., E.C.G. and M.E.G. advised on the study. S.H., E.C.G. and M.E.G. obtained funding for the research. S.H., S.S., E.C.G. and M.E.G. wrote the manuscript.

Competing interests S.A. is the founder and CEO of Neurophotometrics Ltd., which manufactures fibre photometry systems. All other authors declare no competing interests.

Additional information

Supplementary information is available for this paper at https://doi.org/10.1038/s41586-020-2387-5.
Correspondence and requests for materials should be addressed to S.H. or M.E.G.
Peer review information *Nature* thanks Trygve E. Bakken, Shaun F. Morrison and the other, anonymous, reviewer(s) for their contribution to the peer review of this work.
Reprints and permissions information is available at http://www.nature.com/reprints.

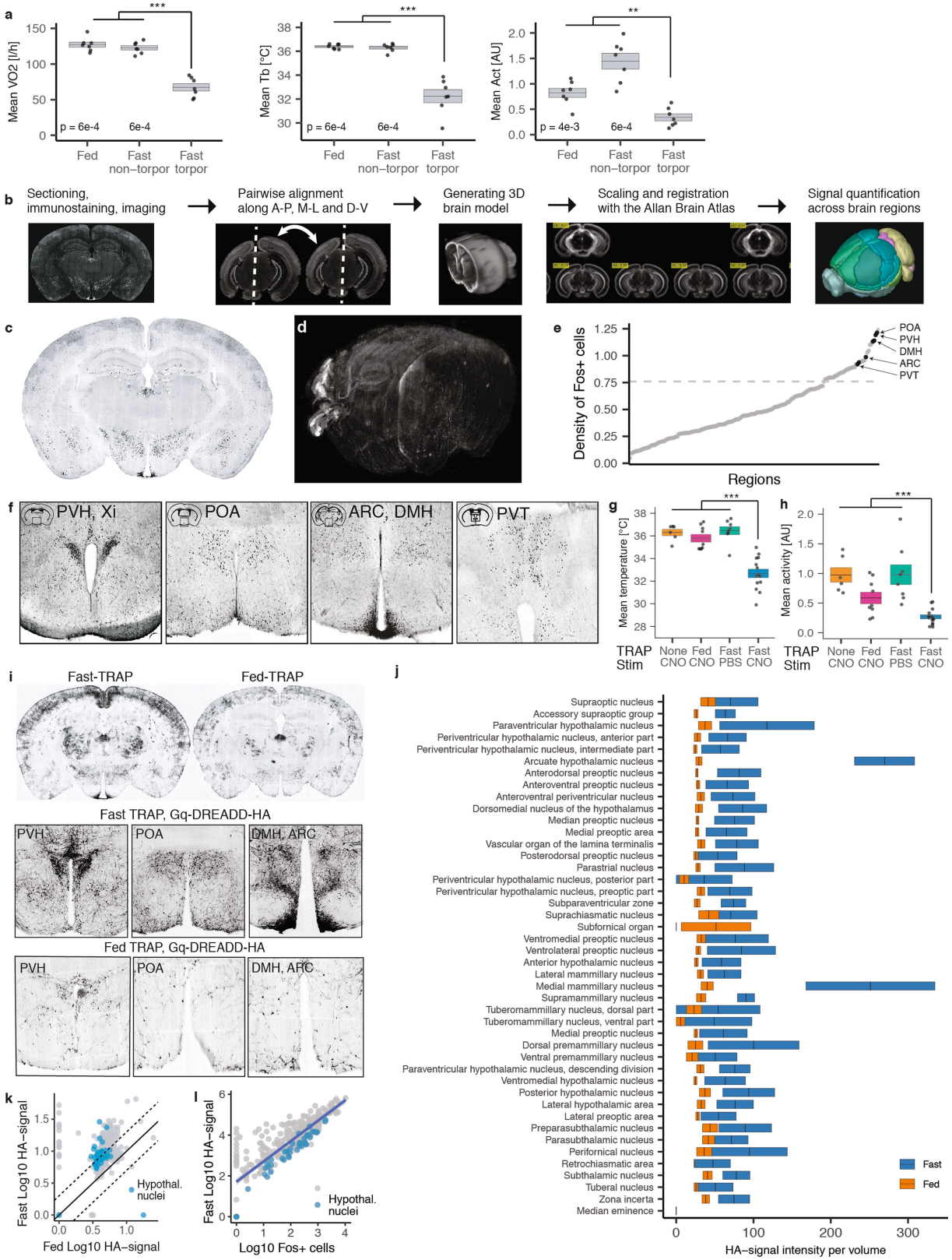

Extended Data Fig. 1 | See next page for caption.

Extended Data Fig. 1 | Torpor metabolic rate, brain-wide search for torpor-regulating cells and chemogenetic reactivation of FosTRAP-Gq mice. **a**, Mean metabolic rate (VO_2), body temperature (T_b) and gross motor activity (Act) of mice in torpor compared to mice that are fed or fasted yet not in torpor ($n = 7$, P values indicated on the graph). **b**, Schematic for the whole-brain reconstruction of FOS staining. **c**, Example brain slice showing Fos staining in a fasted torpid mouse (representative of $n = 3$ mice). **d**, 3D-reconstructed Fos-stained brain slices from a fasted torpid mouse. **e**, Average density of FOS^+ cells (number of cells divided by the volume of the region, $n = 3$ mice, see Methods) across 179 brain regions that had on average at least 100 FOS^+ cells. Paraventricular hypothalamus (PVH), a subregion of the preoptic area (POA), arcuate nucleus (ARC), dorsomedial hypothalamus (DMH) and paraventricular thalamus (PVT) are indicated. **f**, FOS staining of the PVH, xiphoid nucleus (Xi), POA, ARC, DMH and PVT of fasted torpid mice ($n = 3$ mice). **g**, Mean core body temperature (T_b) over 4 h after CNO administration is significantly lower in torpor-TRAP ($n = 14$ mice) compared to non-TRAP ($n = 6$ mice, $P = 5.2 \times 10^{-5}$) and fed-TRAP ($n = 9$ mice, $P = 2.9 \times 10^{-5}$) mice and compared to torpor-TRAP mice injected with PBS ($n = 8$ mice, $P = 2.5 \times 10^{-5}$). **h**, Mean activity over 4 h after CNO administration is significantly lower in torpor-TRAP ($n = 14$ mice) compared to non-TRAP ($n = 6$ mice, $P = 5.2 \times 10^{-5}$) and fed-TRAP ($n = 9$ mice, $P = 9.8 \times 10^{-3}$) mice and compared to torpor-TRAP mice injected with PBS ($n = 8$ mice, $P = 2.5 \times 10^{-5}$). **i**, Coronal brain sections from FosTRAP, LSL-Gq-DREADD-HA mice TRAPed during fasting-induced torpor (fast-TRAP, $n = 2$ mice) or in a fed state (fed-TRAP, $n = 4$ mice) and immunostained for HA. Staining in selected brain areas (PVH, POA, ARC, DMH and PVT) is shown. **j**, Volume-normalized signal intensity of HA staining across different hypothalamic nuclei in four fed-TRAP and two fast-TRAP mice. **k**, Brain-wide quantification of HA staining from four fed-TRAP and two fast-TRAP mice. Numerous (190/316) brain regions, including 32 hypothalamic areas, show increased Gq-DREADD-HA expression (>2-fold) in fast-TRAP mice compared to fed-TRAP mice. The solid line indicates unity, dashed lines indicate twofold differences. **l**, Correlation across brain regions between the number of FOS^+ cells in torpid mice and the levels of Gq-DREADD expression in fast-TRAP mice ($R = 0.83$, $P = 2.2 \times 10^{-16}$, Pearson correlation test, $n = 316$ regions). All box plots indicate mean ± s.e.m. All P values are calculated using two-tailed Mann–Whitney U-tests, $^{**}P < 0.01$, $^{***}P < 0.001$.

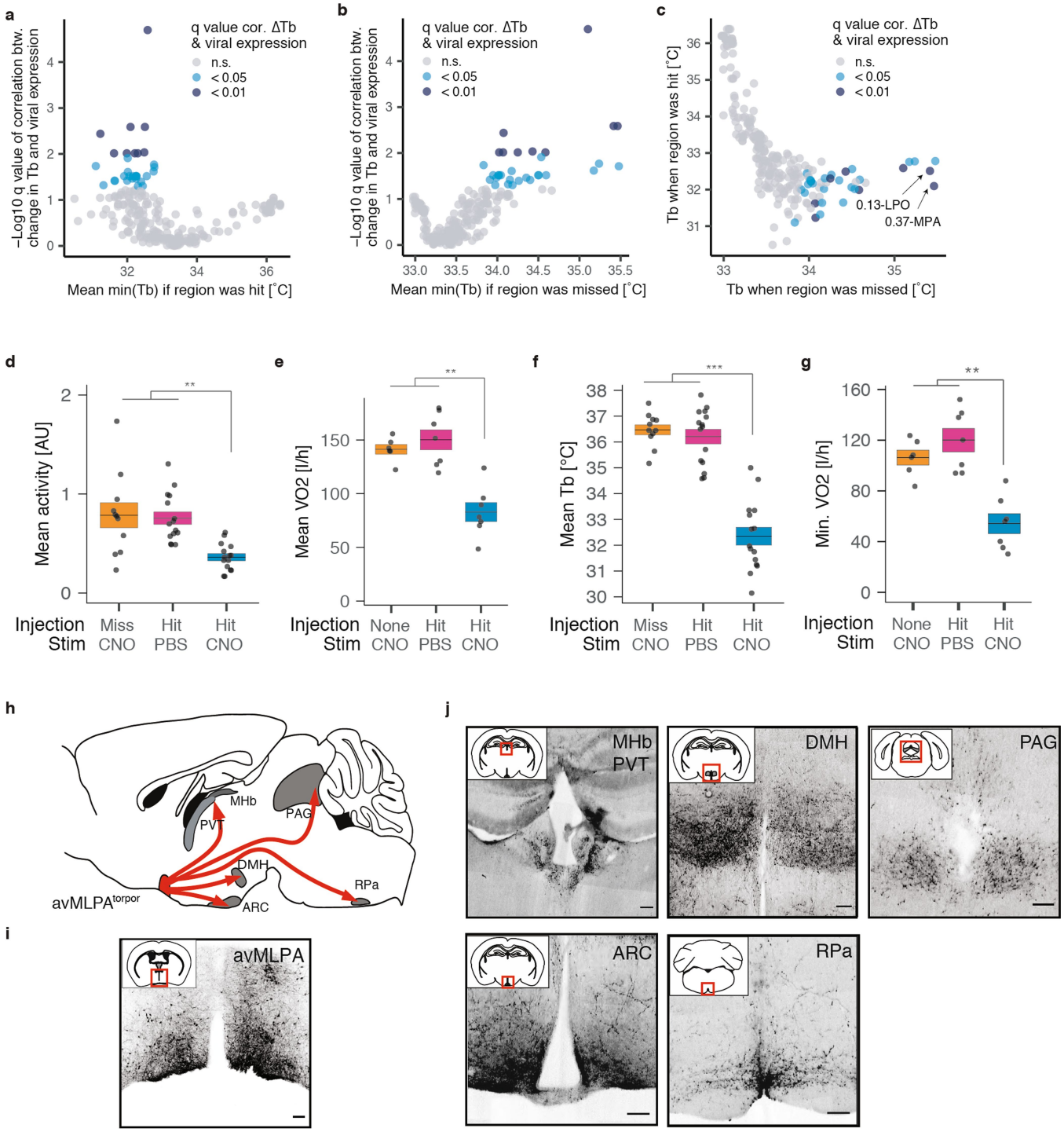

Extended Data Fig. 2 | See next page for caption.

Extended Data Fig. 2 | Chemogenetic reactivation of torpor-TRAPed neurons in different hypothalamic regions and anterograde projections of torpor-TRAPed avMLPA neurons. a–**c**, AAV-DIO-Gq–mCherry was injected into different hypothalamic regions of FosTRAP mice ($n = 54$ mice). After TRAPing during torpor, we administered CNO and measured the effect of the reactivation of torpor-TRAPed neurons within the virally injected region on core body temperature. All mice were euthanized, and the expression of the virally derived Gq-DREADD–mCherry was evaluated in each mouse across 277 hypothalamic nuclei. **a**, **b**, Each circle represents one of the 277 hypothalamic nuclei, and the *y* axis represents the $-\log_{10}$ FDR-corrected *q* value of the Pearson correlation (across 54 mice, *q* values displayed in Supplementary Table 3) between the viral expression in that nucleus and the decrease in T_b that was observed after CNO stimulation. Next, for each nucleus, 54 mice were grouped into those in which the nucleus was hit (**a**) and those in which it was missed (**b**). For each of the two groups of mice, the minimum body temperature after CNO administration was averaged and plotted. **c**, For each nucleus and the corresponding two groups of mice, the minimum body temperature after CNO administration was plotted (hit group, *y* axis; missed group, *x* axis). Arrows indicate anterior MPA and LPO regions. When these regions were hit with the virus and the TRAPed neurons were chemogenetically reactivated, the body temperature of the mouse decreased, whereas when these regions were missed the body temperature did not decrease. **d**, Mean activity over 4 h after CNO administration is significantly lower in avMLPA-hit ($n = 15$ mice) compared with avMLPA-missed ($n = 11$ mice, $P = 1.4 \times 10^{-3}$) mice, and compared with avMLPA-hit mice injected with PBS ($n = 15$ mice, $P = 4.8 \times 10^{-6}$). **e**, Mean metabolic rate (VO_2) over 4 h after CNO administration is significantly lower in avMLPA-hit ($n = 7$ mice) compared with non-injected ($n = 6$ mice, $P = 2.3 \times 10^{-3}$) mice or avMLPA-hit mice injected with PBS ($n = 6$ mice, $P = 1.2 \times 10^{-3}$). **f**, Mean core body temperature (T_b) over 4 h after CNO administration is significantly lower in avMLPA-hit ($n = 15$ mice) compared to avMLPA-missed ($n = 11$ mice, $P = 2.6 \times 10^{-7}$) mice or avMLPA-hit mice injected with PBS ($n = 15$ mice, $P = 9.0 \times 10^{-8}$). **g**, Minimum metabolic rate (VO_2) over 4 h after CNO administration is significantly lower in avMLPA-hit ($n = 7$ mice) compared with non-injected ($n = 6$ mice, $P = 2.3 \times 10^{-3}$) mice or avMLPA-hit mice injected with PBS ($n = 6$ mice, $P = 1.2 \times 10^{-3}$). **h**, Schematic showing projections of TRAPed avMLPA^{torpor} neurons. **i**, **j**, Gq-DREADD–mCherry fusion protein expression was used to visualize the projection of TRAPed avMLPA^{torpor} neurons across the brain ($n = 4$ mice). **i**, Expression of mCherry near the injection site (avMLPA). **j**, Representative images of projections to the medial habenula (MHb), PVT, DMH, periaqueductal grey (PAG), ARC and raphe pallidus (RPa). Scale bars, 50 µm. For the box plots, the centre line and box boundaries indicate mean ± s.e.m. All *P* values were calculated using a two-tailed Mann–Whitney *U*-test, $^{**}P < 0.01$, $^{***}P < 0.001$.

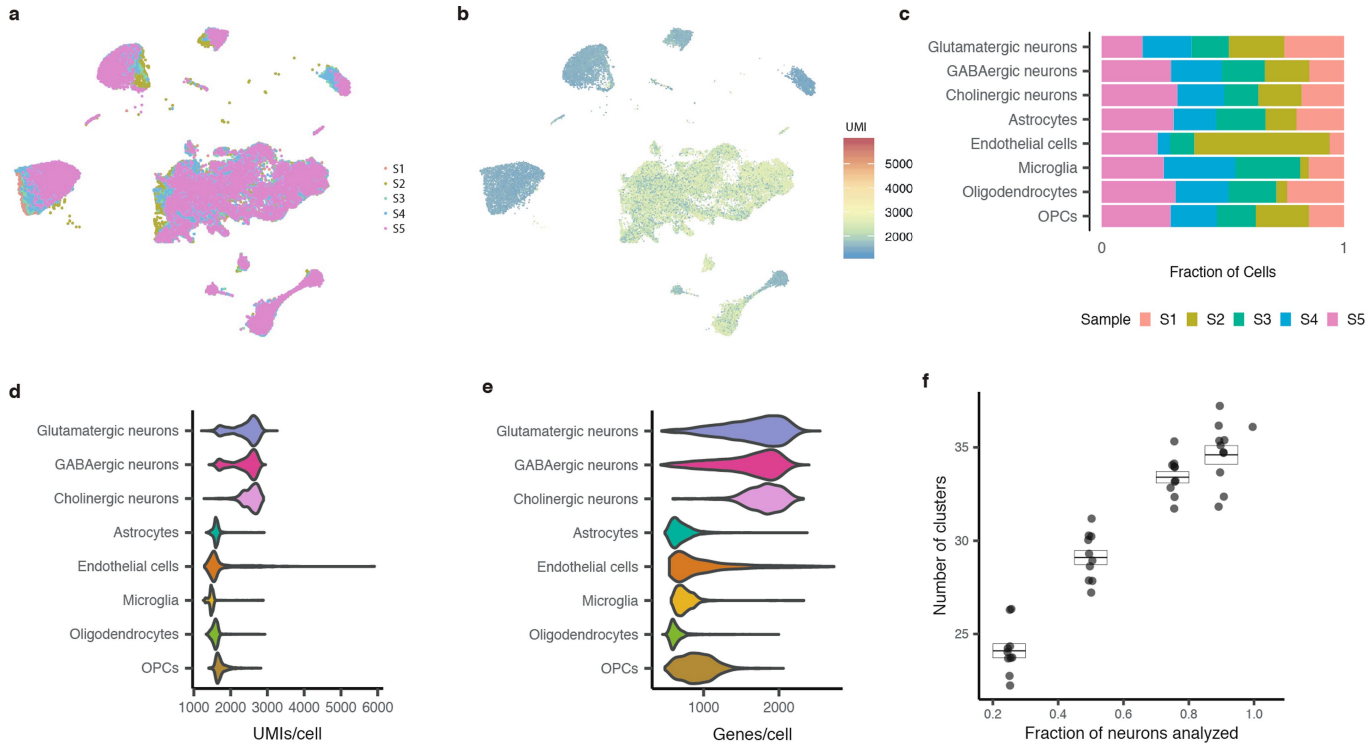

Extended Data Fig. 3 | snRNA-seq metrics. a, **b**, UMAP plot of 39,562 nuclei from the avMLPA of five mice, in which the colours denote cells derived from each mouse (**a**) or the number of unique transcripts (UMI) per nucleus (**b**). **c**, Relative contribution of each sample ($n = 5$ mice) towards the total cell population making up each main cell class. **d**, Violin plot of the distribution of UMIs per cell for each main cell class (glutamatergic neurons, $n = 11,275$ cells; GABAergic neurons, $n = 16,307$ cells; cholinergic neurons, $n = 521$ cells; astrocytes, $n = 3,479$ cells; endothelial cells, $n = 421$ cells; microglia, $n = 1,247$ cells; oligodendrocytes, $n = 4,718$ cells; and OPCs, $n = 1,594$ cells). **e**, Violin plot of the distribution of genes per cell for each main cell class. **f**, Number of neuronal clusters formed when different fractions (25%, 50%, 75% and 90%) of total neurons ($n = 7,025, 14,051, 21,077$ and $25,292$, respectively) are used for clustering. For each fraction a random subset of neurons was used and the analysis was repeated ten times. For the box plots, the centre line and box boundaries indicate mean ± s.e.m, and the violin plot shows the distribution from the lowest to the largest value.

Extended Data Fig. 4 | Marker gene expression across neuronal cell types. The colour denotes mean expression across all nuclei normalized to the highest mean across cell types, and the size represents the fraction of nuclei in which the marker gene was detected. Cell types are organized on the basis of hierarchical clustering across all variable genes. The five most unique makers are identified and plotted for each cell type unless a marker was identified across multiple cell types, in which case it was plotted only once.

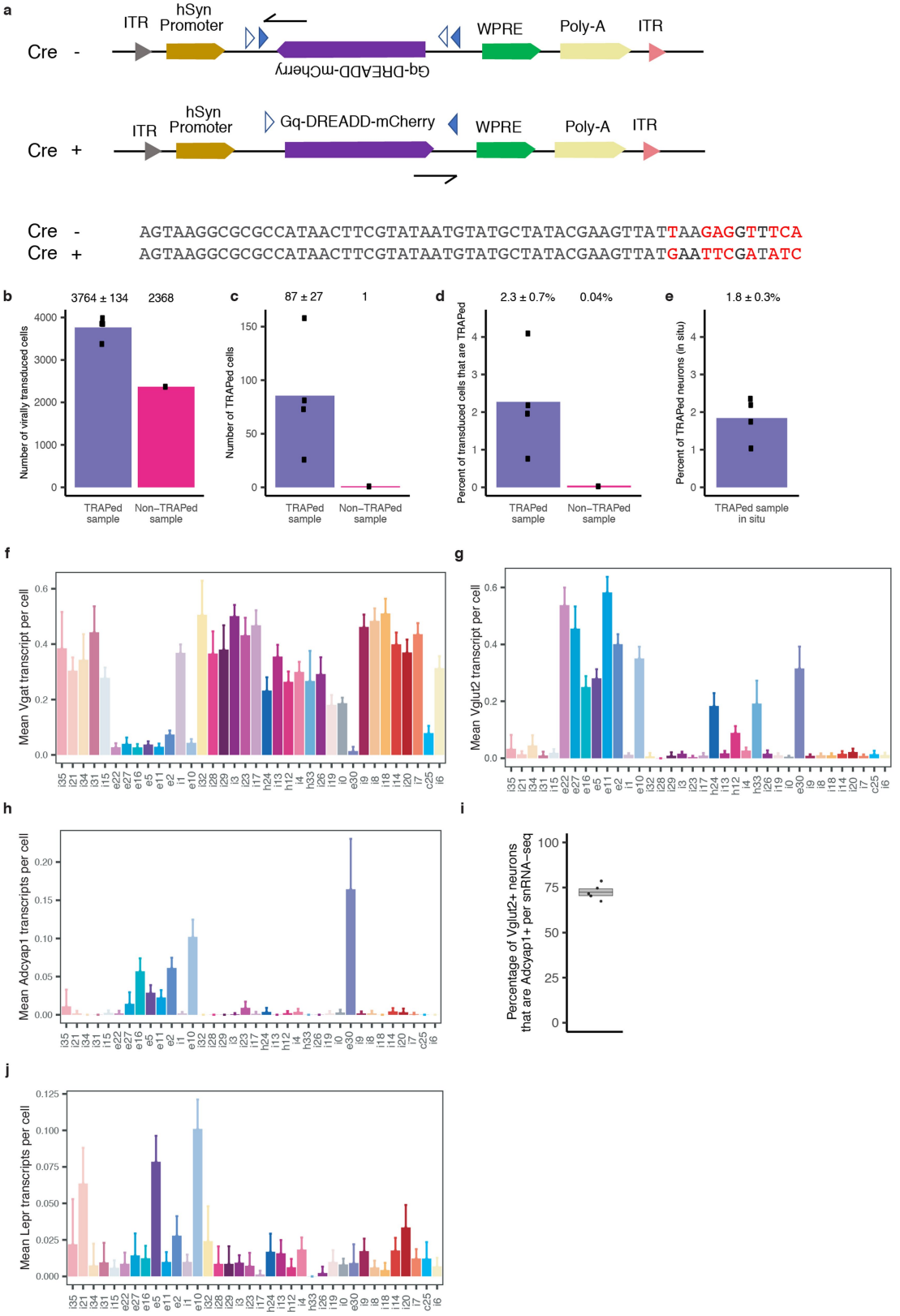

Extended Data Fig. 5 | See next page for caption.

Extended Data Fig. 5 | Strategy for identifying TRAPed torpor-regulating neurons via snRNA-seq and gene expression of marker genes in the avMLPA. a, Schematic for the identification of Cre-dependent AAV-DIO-Gq-DREADD–mCherry mRNA with or without recombination. Top, AAV-DIO-Gq-DREADD–mCherry vector map before (Cre^-) and after (Cre^+) Cre-mediated recombination. Blue and white triangles surrounding the Gq-GREADD–mCherry indicate *loxP* sites. Black arrows indicate the binding site of the sequencing primer. ITR, inverted terminal repeats; WPRE, Woodchuck Hepatitis Virus post-transcriptional regulatory element; Poly-A, polyadenylation signal. Bottom, owing to the Cre-mediated inversion in the AAV-DIO-Gq-DREADD–mCherry vector, the mRNA transcript sequence 3′ of the sequencing primer is different after Cre-mediated recombination, enabling us to identify TRAPed cells during snRNA-seq as those cells in which the viral mRNA contains the recombined (Cre^+) sequence. **b**, Quantification of the number of virally transduced cells in TRAPed ($n = 4$ mice) and non-TRAPed ($n = 1$ mouse) samples. **c**, Quantification of the number of TRAPed cells in TRAPed (86 ± 27 cells) and non-TRAPed (1 cell) samples. **d**, The percentage of transduced cells that are TRAPed in TRAPed (2.3 ± 0.7%, $n = 4$ mice) and non-TRAPed (0.04%, $n = 1$ mouse) samples based on snRNA-seq analysis. **e**, The percentage of TRAPed neurons in TRAPed samples (1.8 ± 0.3%, $n = 4$ mice) based on fluorescence in situ hybridization analysis. **f**–**h**, Mean transcripts per cell across all neuronal cell types identified in snRNA-seq for *Vgat* (*Slc32a1*, marker of GABAergic neurons) (**f**), *Vglut2* (*Slc17a6*, marker of glutamatergic neurons) (**g**) and *Adcyap1* (adenylate cyclase-activating peptide 1) (**h**). **i**, snRNA-seq indicates that e2, e5, e10, e11, 16 and e30 represent $Vglut2^+Adcyap1^+$ cell types, whereas e22, e27, h33, h12 and h24 are $Vglut2^+Adcyap1^-$. On the basis of this categorization, 72.4 ± 2.2% of $Vglut2^+$ neurons are $Adcyap1^+$ ($n = 5$ mice). For the box plot, the centre line and box boundaries indicate mean ± s.e.m. **j**, Mean transcripts per cell across all neuronal cell types identified in snRNA-seq for *Lepr*. $Adcyap1^+$ clusters e5 and e10 express *Lepr*. Data are mean ± 2s.e.m.

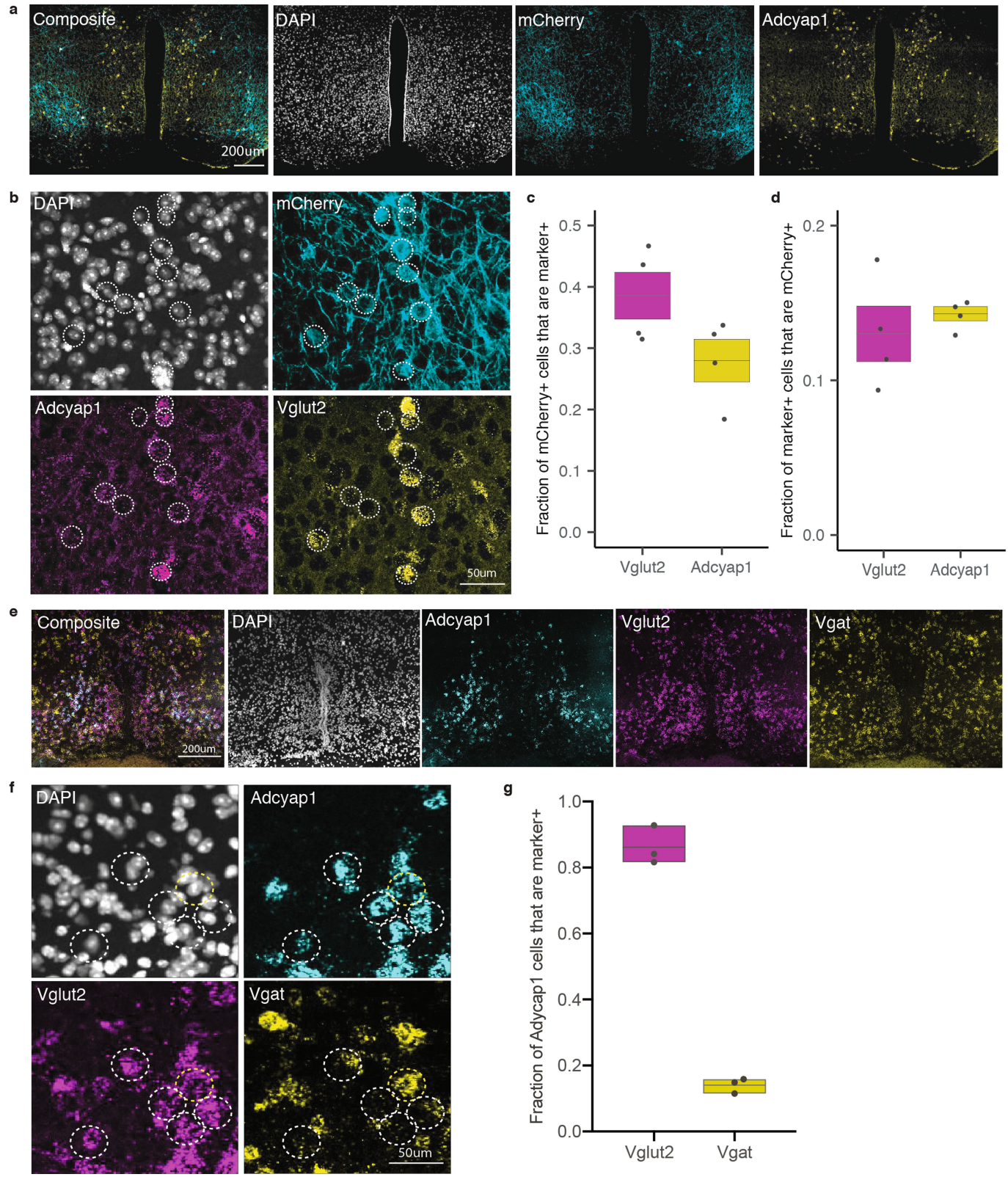

Extended Data Fig. 6 | See next page for caption.

Extended Data Fig. 6 | In situ hybridization analysis of torpor-regulating avMLPA neurons. a, Coronal sections showing the avMLPA of FosTRAP mice ($n = 4$ mice) injected with AAV-DIO-Gq-DREADD–mCherry and torpor-TRAPed. Immunofluorescent staining against mCherry indicates the location of avMLPA^{torpor} neurons (cyan), whereas in situ hybridization indicates the expression of the marker gene *Adcyap1*. **b**, High-magnification images of staining shown in **a** indicate the location of mCherry^{+} avMLPA^{torpor} neurons (cyan), whereas in situ hybridization indicates the expression of marker genes *Adcyap1* and *Vglut2*. Example avMLPA^{torpor} mCherry^{+} cells are circled. Several mCherry^{+} cells express *Adcyap1* and/or *Vglut2*. **c**, Quantification of the fraction of avMLPA^{torpor} neurons that express *Adcyap1* (28.8 ± 3.5%, $n = 4$ mice) and *Vglut2* (38.5 ± 3.8%, $n = 4$ mice). **d**, Quantification of the fraction of avMLPA$^{Adcyap1+}$ (14.3 ± 0.5%, $n = 4$ mice) and avMLPA$^{Vglut2+}$ (13.0 ± 1.8%, $n = 4$ mice) neurons that are torpor-TRAPed. **e**, Coronal section showing the avMLPA of FosTRAP mice. In situ hybridization shows cells that are positive for *Adcyap1* (cyan), *Vgat* (yellow) and *Vglut2* (purple). The composite image indicates co-expression of multiple markers. **f**, High-magnification image with example *Adcyap1*$^{+}$ cells circled. White circles indicate *Adcyap1*$^{+}$ cells that are positive for *Vglut2* and negative for *Vgat*, whereas yellow circles indicate all *Adcyap1*$^{+}$ cells that are positive for *Vgat* (even if co-positive with *Vglut2*). **g**, The fraction of *Adcyap1*$^{+}$ cells that are positive for *Vglut2* or *Vgat* (82 ± 3% or 14 ± 1%, respectively, $n = 3$ mice). For the box plots, the centre line and box boundaries indicate mean ± s.e.m.

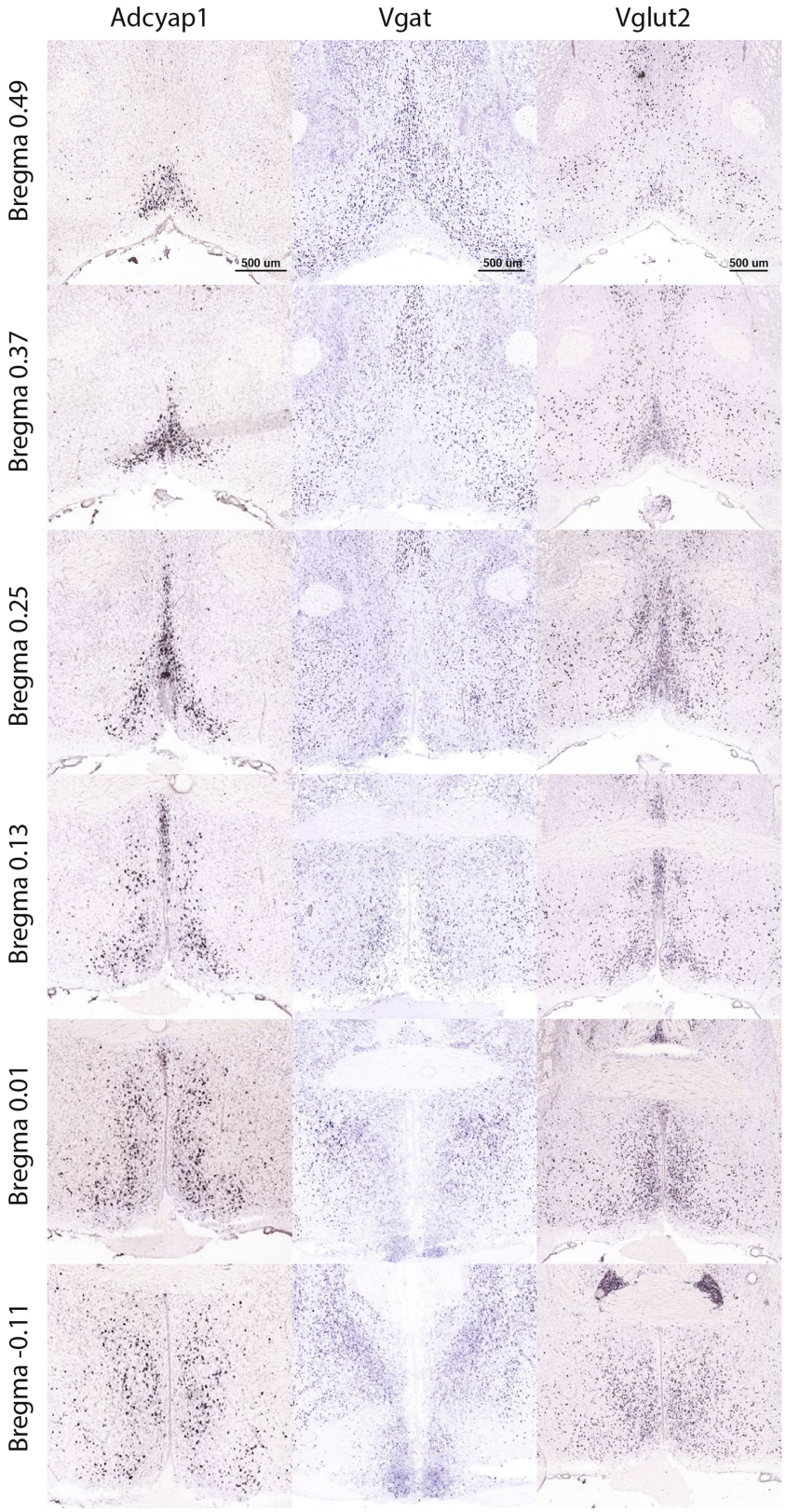

Extended Data Fig. 7 | Expression pattern of *Vgat*, *Vglut2* and *Adcyap1* in the anterior POA. Coronal sections adapted from the Allen Mouse Brain Atlas[32]. Anterior–posterior coordinates relative to bregma are indicated for each set of images.

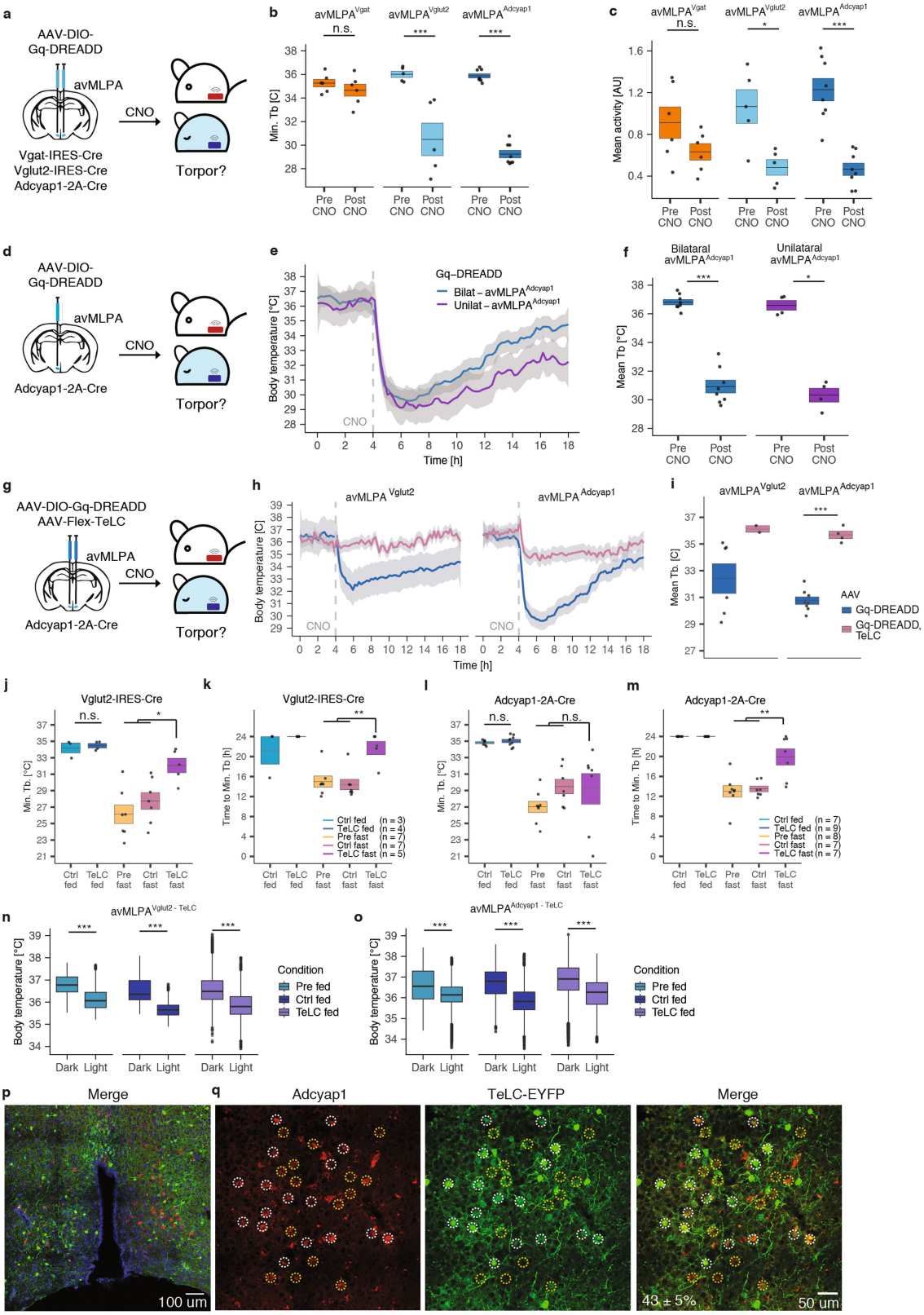

Extended Data Fig. 8 | See next page for caption.

Extended Data Fig. 8 | Chemogenetic stimulation and silencing of avMLPA^{Vgat}, avMLPA^{Vglut2} or avMLPA^{Adcyap1} neurons. a–**c**, Stereotaxic viral injection of AAV-DIO-Gq-DREADD and subsequent chemogenetic stimulation of avMLPA^{Vgat} ($n = 6$ mice), avMLPA^{Vglut2} ($n = 5$ mice) or avMLPA^{Adcyap1} ($n = 8$ mice) neurons. **a**, Experimental schematic. **b**, Minimum core body temperature of avMLPA^{Vgat} mice (orange, $P = 0.48$), avMLPA^{Vglut2} mice (light blue, $P = 8 \times 10^{-3}$) and avMLPA^{Adcyap1} mice (dark blue, $P = 1.6 \times 10^{-4}$) before and after chemogenetic stimulation with CNO. **c**, Mean activity of the same avMLPA^{Vgat} mice ($P = 0.24$), avMLPA^{Vglut2} mice ($P = 0.032$) and avMLPA^{Adcyap1} mice ($P = 1.6 \times 10^{-4}$), before and after chemogenetic stimulation with CNO. **d**, Schematic showing the unilateral stereotaxic viral injection of AAV-DIO-Gq-DREADD and subsequent chemogenetic stimulation of avMLPA^{Adcyap1} neurons. **e**, Change in mean core body temperature after bilateral ($n = 8$ mice) and unilateral ($n = 4$ mice) chemogenetic stimulation of avMLPA^{Adcyap1} neurons. The dashed line indicates CNO administration. Coloured lines indicate the mean core body temperature across mice; grey shading indicates the 95% confidence interval. **f**, Mean core body temperature of mice before and after bilateral ($n = 8$ mice, $P = 1.6 \times 10^{-4}$) or unilateral ($n = 4$ mice, $P = 0.03$) chemogenetic stimulation of avMLPA^{Adcyap1} neurons. **g**, Schematic for the stereotaxic viral co-injection of AAV-Flex-TeLC and AAV-DIO-Gq-DREADD and subsequent chemogenetic stimulation of avMLPA^{Vglut2} and avMLPA^{Adcyap1} neurons. **h**, Changes in mean core body temperature after chemogenetic stimulation of avMLPA^{Vglut2} and avMLPA^{Adcyap1} neurons that either express the excitatory Gq-DREADD receptor ($n = 6$ and $n = 8$ mice, respectively) or co-express the Gq-DREADD receptor and TeLC, which inhibits synaptic transmission ($n = 2$ and $n = 4$ mice, respectively). The dashed line indicates CNO administration. Coloured lines indicate the mean core body temperature across mice; grey shading indicates the 95% confidence interval. **i**, Quantification of mean core body temperature over 4 h after chemogenetic stimulation in avMLPA^{Vglut2} and avMLPA^{Adcyap1} ($P = 1 \times 10^{-6}$) neurons that either solely express the excitatory Gq-DREADD receptor ($n = 6$ and $n = 8$ mice, respectively) or co-express the Gq-DREADD and TeLC ($n = 2$ and $n = 4$ mice, respectively). **j**–**o**, Stereotactic injection of AAV-Flex-TeLC to inhibit synaptic transmission in avMLPA^{Vglut2} and avMLPA^{Adcyap1} neurons. **j**, **k**, Core body temperature of fed and fasted Vglut2-IRES-Cre mice from Fig. 4e (the number of mice in each group is indicated on the graph). **j**, The minimum T_b is not significantly different between control-fed and TeLC-fed ($P = 0.72$) mice, but is significantly lower in control-fast ($P = 0.018$), and pre-fast ($P = 0.01$) compared to TeLC-fast mice, suggesting that avMLPA^{Vglut2} activity is necessary for torpor. **k**, Time needed to reach the minimum body temperature (Fig. 4e) is significantly longer in TeLC-fast compared with either pre-fast or control-fast mice ($P = 9.2 \times 10^{-3}$ for both sets). **l**, **m**, Body temperature of fed and fasted Adcyap1-2A-Cre mice from Fig. 4f (the number of mice in each group is indicated on the graph). **l**, The minimum T_b is not significantly different between control-fed and TeLC-fed ($P = 0.41$) mice, or in TeLC-fast compared to control-fast ($P = 0.71$) and pre-fast ($P = 0.19$) mice. **m**, Time needed to reach the minimum body temperature (Fig. 4f) is significantly longer in TeLC-fast compared to pre-fast ($P = 2 \times 10^{-3}$) and control-fast ($P = 7 \times 10^{-3}$) mice. **n**, **o**, Core body temperature (measured in 1-min intervals) of fed mice during the 12-h light and 12-h dark cycle in which avMLPA^{Vglut2} (**n**) or avMLPA^{Adcyap1} (**o**) neurons were injected with either AAV-Flex-TeLC (TeLC), a control AAV (control), or remained un-injected (Pre). The core body temperature is significantly different between the dark and light cycle across pre-fed ($n = 3$ mice, $n = 3{,}960$ temperature data points, $P = 2 \times 10^{-16}$), control-fed ($n = 2$ mice, $n = 2{,}640$ temperature data points, $P = 2 \times 10^{-16}$) and TeLC-fed ($n = 5$ mice, $n = 6{,}600$ temperature data points, $P = 2 \times 10^{-16}$) Vglut2-IRES-Cre mice (**n**) as well as pre-fed ($n = 4$ mice, $n = 5{,}280$ temperature data points, $P = 2 \times 10^{-16}$), control-fed ($n = 7$ mice, $n = 9{,}240$ temperature data points, $P = 2 \times 10^{-16}$) and TeLC-fed ($n = 8$ mice, $n = 10{,}560$ temperature data points, $P = 2 \times 10^{-16}$) Adcyap-2A-Cre mice (**o**). In the box plots the centre line denotes the median, the box boundaries mark the interquartile range (IQR) and the whiskers extend to 1.5 × IQR and any data points outside this range. **p**, **q**, Coronal section showing the avMLPA of Adcyap1-2A-Cre mice ($n = 2$ mice) injected with AAV-Flex-TeLC-eYFP. Immunofluorescent staining against eYFP indicates the location of silenced TeLC$^+$ neurons (green), whereas in situ hybridization indicates the expression of the *Adcyap1* mRNA. **q**, High-magnification image with example *Adcyap1*$^+$ cells circled. White circles indicate *Adcyap1*$^+$ cells that co-express TeLC–eYFP ($43 \pm 5\%$, $n = 2$ mice), yellow circles indicate *Adcyap1*$^+$ that do not co-express TeLC–eYFP. All *P* values are calculated using a two-tailed Mann–Whitney *U*-test. NS indicates not statistically significant, $^*P < 0.05$, $^{**}P < 0.01$, $^{***}P < 0.001$. In the box plots in **b**–**m**, the centre line and box boundaries indicate mean ± s.e.m.

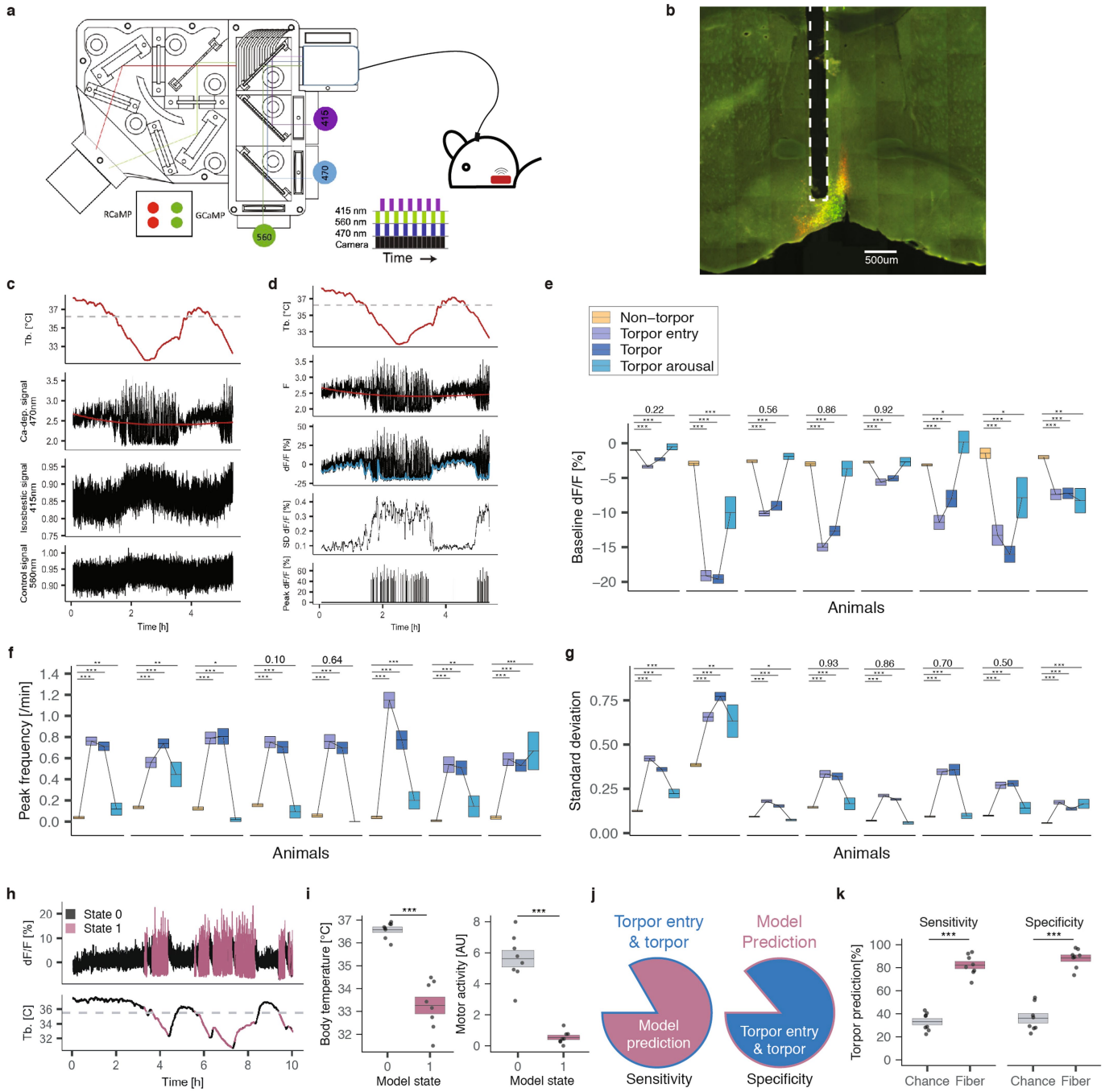

Extended Data Fig. 9 | See next page for caption.

Extended Data Fig. 9 | Fibre-photometry set-up, recordings and torpor model. a, Schematic showing the fibre-photometry set-up. Three LED lights (415 nm, 470 nm and 560 nm) were used as excitation light sources. For all recordings, 470 nm and 560 nm light sources were driven in phase, with 415 nm driven out of phase (Methods). The emitted signals were detected by a digital camera at the end of a patch cord. **b**, Example coronal brain slice from an Adcyap1-2A-Cre mouse co-injected with AAV-DIO-Gq-DREADD–mCherry and AAV-Flex-GCaMP6s and used for fibre photometry studies ($n = 8$ mice). The white dashed lines indicate the location of the optical fibre. Cells co-expressing GCaMP6s (green) and mCherry (red) appear yellow. **c**, Example fibre-photometry recording (from mouse shown in **b**) showing the core body temperature (top) followed by three different signals (470 nm, 415 nm and 560 nm). Here, the 470-nm signal represents the calcium-dependent GCaMP6s signal, the 415-nm signal represents the Ca^{2+}-independent isosbestic GCaMP6s signal, and the 560-nm signal represents the mCherry signal. The red line indicates the scaled fit of the Ca^{2+}-independent 415-nm signal used to normalize the Ca^{2+}-dependent 470-nm signal for Ca^{2+}-independent changes in signal intensity. Both the 415-nm and 560-nm channels serve as controls for heat-mediated LED decay, bleaching of GCaMP6s and movement artefacts. **d**, Recordings of a representative fasting session. Top panel, core body temperature of mice during each recording session (dashed line indicates the threshold body temperature below which the mouse is considered torpid); second panel, raw Ca^{2+}-dependent 470-nm GCaMP6s signal (the red line indicates the scaled fit of the Ca^{2+}-independent 415-nm signal used to normalize for bleaching or other Ca^{2+}-independent changes in signal intensity); third panel, dF/F value relative to the Ca^{2+}-independent scaled fit (blue line indicates the local baseline, which is determined as the 10th percentile of the dF/F value within a sliding three-minute interval); fourth panel, the standard deviation of the dF/F value calculated within a sliding three-minute interval; bottom panel, the dF/F values of the most prominent peaks identified (top 1% of all peaks in the session). **e**–**g**, Quantification of baseline dF/F (%) (**e**), peak frequency (per min) (**f**) and standard deviation (**g**) for non-torpid (yellow), torpor entry (light blue), torpor (blue) and torpor arousal (teal) in 8 individual mice across all 3-min intervals (left to right: $n = 251, 62, 97, 17, 321, 46, 57, 15, 203, 52, 39, 19, 269, 44, 66, 18, 141, 30, 59, 2, 250, 57, 42, 5, 43, 31, 23, 7, 80, 44, 51, 8$ time intervals). In box plots, the centre line and box boundaries indicate mean ± s.e.m. P values greater than 0.05 are indicated. **h**, Example fibre-photometry signal (top) clustered into two states and coloured by state. State 0 corresponds to the mouse being out of torpor or exiting torpor, whereas state 1 corresponds to the mouse entering or maintaining torpor. **i**, Core body temperature (left) and motor activity (right) are significantly lower during state 1 compared with state 0 of the photometry-based model ($n = 8$ mice, $P = 1.6 \times 10^{-4}$). **j**, The time that a mouse spent in torpor (entry or maintenance) was accurately calculated by the model based on the photometry data 82.3 ± 3.2% of the time (model sensitivity). Conversely, whenever the model determined that the mouse was entering or maintaining torpor, its estimation was 88.4 ± 2.8% accurate (specificity). **k**, Model sensitivity and specificity were significantly lower ($P = 1.6 \times 10^{-4}$, $n = 8$ mice) when the temporal relationship between the temperature and the fibre-photometry data was removed. In box plots, the centre line and box boundaries indicate mean ± s.e.m. All P values were calculated using a two-tailed Mann–Whitney U-test. $^{*}P < 0.05$, $^{**}P < 0.01$, $^{***}P < 0.001$.

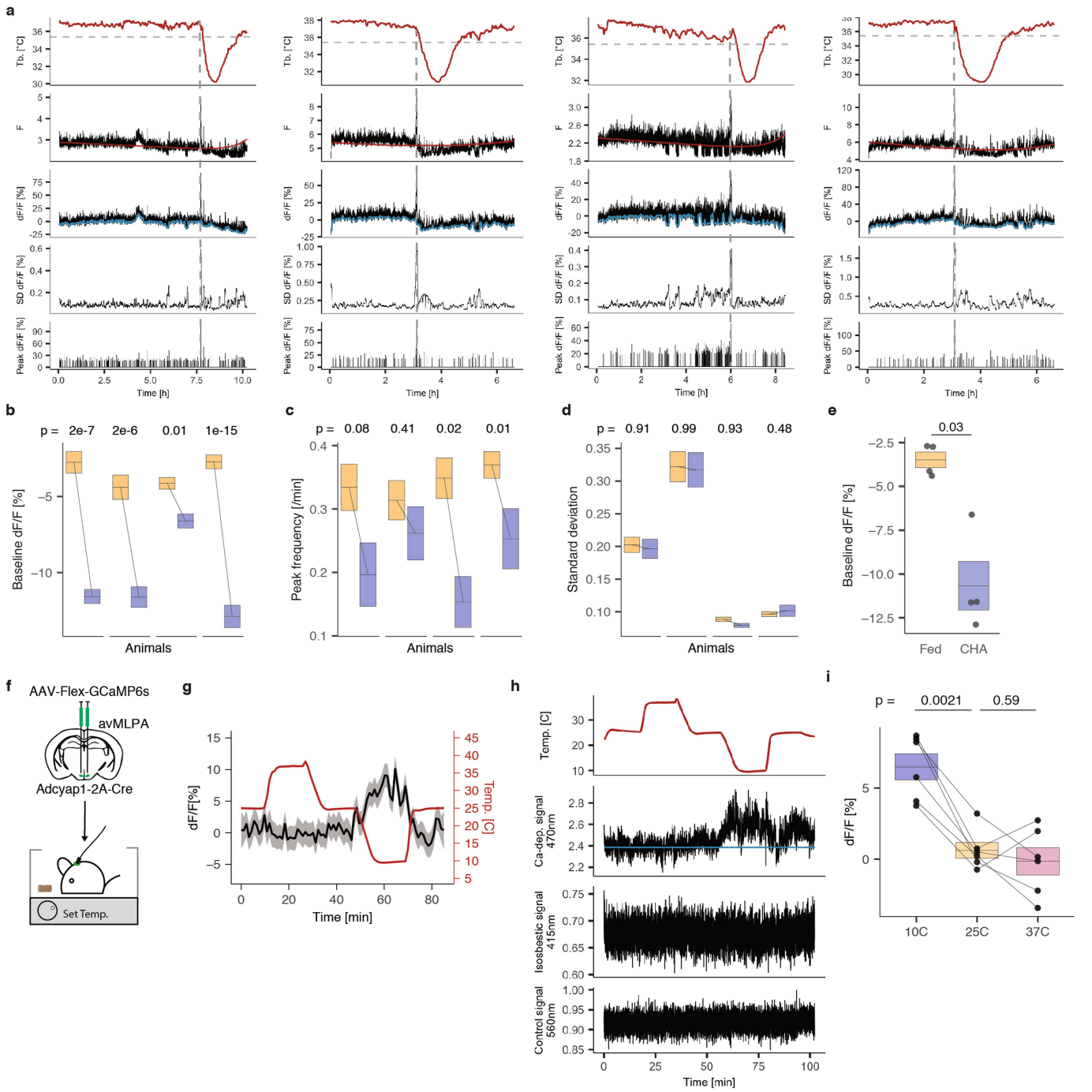

Extended Data Fig. 10 | Fibre-photometry recordings of avMLPA^{Adcyap1} neurons in fed freely moving mice with CHA-induced hypothermia and changes in ambient temperature. a, Fibre-photometry recording data displayed as in Extended Data Fig. 9d. The dashed line indicates the time of CHA administration. **b**–**d**, Baseline d*F*/*F* (**b**), peak frequency (**c**) and standard deviation (**d**) measured for each mouse before and after CHA administration across all recorded three-minute intervals (left to right: $n = 69, 17, 63, 23, 140, 24, 161$ and 37 time intervals). **e**, The mean baseline decreases after CHA treatment ($P = 0.03$, $n = 4$ mice). **f**, Schematic showing the fibre-photometry recording of avMLPA^{Adcyap1} neurons when mice are exposed to different environmental temperatures with food provided in the chamber. **g**, Mean GCaMP6s signal ($n = 6$ mice) of avMLPA^{Adcyap1} neurons with environmental temperature changes along a programmed sequence: 25 °C → 37 °C → 25 °C → 10 °C → 25 °C. Grey shading indicates the 95% confidence interval. **h**, Example fibre-photometry recording showing the ambient (chamber) temperature (top) followed by three different signals (470 nm, 415 nm and 560 nm). Signals from the 415-nm and 560-nm channels are used as controls for any potential effects of temperature on the photometry signal. **i**, Mean neuronal responses at different ambient temperatures. avMLPA^{Adcyap1} neurons are not sensitive to increases in the ambient temperature to 37 °C ($P = 0.59$), and instead appear to be sensitive to a decrease in environmental temperature ($n = 6$ mice, $P = 0.0021$). In box plots, the centre line and box boundaries indicate mean ± s.e.m. All *P* values were calculated using a two-tailed Mann–Whitney *U*-test. NS indicates not statistically significant, $^{*}P < 0.05$, $^{**}P < 0.01$, $^{***}P < 0.001$.

nature research

Corresponding author(s): Michael Greenberg, Sinisa Hrvatin

Last updated by author(s): May 1, 2020

Reporting Summary

Nature Research wishes to improve the reproducibility of the work that we publish. This form provides structure for consistency and transparency in reporting. For further information on Nature Research policies, see Authors & Referees and the Editorial Policy Checklist.

Statistics

For all statistical analyses, confirm that the following items are present in the figure legend, table legend, main text, or Methods section.

n/a	Confirmed	
☐	☒	The exact sample size (*n*) for each experimental group/condition, given as a discrete number and unit of measurement
☐	☐	A statement on whether measurements were taken from distinct samples or whether the same sample was measured repeatedly
☐	☒	The statistical test(s) used AND whether they are one- or two-sided *Only common tests should be described solely by name; describe more complex techniques in the Methods section.*
☐	☐	A description of all covariates tested
☐	☒	A description of any assumptions or corrections, such as tests of normality and adjustment for multiple comparisons
☐	☐	A full description of the statistical parameters including central tendency (e.g. means) or other basic estimates (e.g. regression coefficient) AND variation (e.g. standard deviation) or associated estimates of uncertainty (e.g. confidence intervals)
☐	☐	For null hypothesis testing, the test statistic (e.g. *F*, *t*, *r*) with confidence intervals, effect sizes, degrees of freedom and *P* value noted *Give P values as exact values whenever suitable.*
☐	☐	For Bayesian analysis, information on the choice of priors and Markov chain Monte Carlo settings
☐	☐	For hierarchical and complex designs, identification of the appropriate level for tests and full reporting of outcomes
☐	☐	Estimates of effect sizes (e.g. Cohen's *d*, Pearson's *r*), indicating how they were calculated

Our web collection on statistics for biologists contains articles on many of the points above.

Software and code

Policy information about availability of computer code

Data collection	VitalView 5.1 (Starr Life Sciences) for collection of body temperature and activity. Oxymax (Columbus Instruments) for CLAMS experiments. Bonsai 2.4 (open-source) for collection of fiber photometry. Olyvia 2.4 (Olympus) for imaging brain sections. LasX 3.3.0 (Leica) for imaging in situs.
Data analysis	Most of the analysis was performed in R. Image processing was performed in Fiji 2.0.0 (converstion to TIFF), Matlab R2019b (MathWorks) and using Riffle Shuffle (github.com/hms-idac/RiffleShuffle). Single nucleus RNA-seq analysis was performed using Cellranger 3.1.0 (10X Genomics), Scublet (python package) and Seurat 3.1 (R package).

For manuscripts utilizing custom algorithms or software that are central to the research but not yet described in published literature, software must be made available to editors/reviewers. We strongly encourage code deposition in a community repository (e.g. GitHub). See the Nature Research guidelines for submitting code & software for further information.

Data

Policy information about availability of data

All manuscripts must include a data availability statement. This statement should provide the following information, where applicable:

- Accession codes, unique identifiers, or web links for publicly available datasets
- A list of figures that have associated raw data
- A description of any restrictions on data availability

The data that support the findings of this study are available from the corresponding author. Raw and processed single-cell RNA-seq counts data and metadata is available at GEO accession GSE149344.

Field-specific reporting

Please select the one below that is the best fit for your research. If you are not sure, read the appropriate sections before making your selection.

☒ Life sciences ☐ Behavioural & social sciences ☐ Ecological, evolutionary & environmental sciences

For a reference copy of the document with all sections, see nature.com/documents/nr-reporting-summary-flat.pdf

Life sciences study design

All studies must disclose on these points even when the disclosure is negative.

Sample size	No statistical methods were used to predetermine sample size. Sample sizes are indicated for each experiment and were chosen based on similar studies.
Data exclusions	Pre-established criteria were used for data inclusion/exclusion. Due to variability across stereotactic injections, only FosTRAP animals that showed a decrease in core body temperature following chemogenetic stimulation were used for snRNA-seq and in situ hybridization. Cell doublets were removed using criteria that is consistent with other publications and is reported in the methods. For fiber photometry experiments, only animals for which we confirmed the correct placement of the fiber were included.
Replication	Each experiment was performed across several animals (numbers indicated in manuscript). Where possible, data from each individual animal is shown in the manuscript indicating the distribution of the results. Stereotactic surgeries were performed by two separate individuals.
Randomization	Assignment of individual mice to different surgical groups and experimental groups was random.
Blinding	The analysis of viral expression across 54 animals and 277 hypothalamic regions was performed blinded to the effect on core body temperature that was previously observed in each animal. Identification of TRAPed neurons (mCherry+ cells) or marker-expressing cells was each performed while staying blinded to the other analysis to avoid bias.

Reporting for specific materials, systems and methods

We require information from authors about some types of materials, experimental systems and methods used in many studies. Here, indicate whether each material, system or method listed is relevant to your study. If you are not sure if a list item applies to your research, read the appropriate section before selecting a response.

Materials & experimental systems

n/a	Involved in the study
☐	☒ Antibodies
☒	☐ Eukaryotic cell lines
☒	☐ Palaeontology
☐	☒ Animals and other organisms
☒	☐ Human research participants
☒	☐ Clinical data

Methods

n/a	Involved in the study
☒	☐ ChIP-seq
☒	☐ Flow cytometry
☒	☐ MRI-based neuroimaging

Antibodies

Antibodies used	1:300 rabbit anti-mCherry antibody (Abcam # ab167453), 1:500 donkey anti-rabbit 568 antibody (Life technologies Cat# AB_2534017), 1:2000 rabbit anti-Fos (Cedarlane # 226003(SY)), 1:1000 rabbit anti-HA (Cell Signaling Technology # 3724S), 1:500 donkey anti-rabbit 647 (Life Technologies # A31573), 1:1000 chicken anti-GFP antibody (Abcam, ab13970), 1:500 donkey anti-chicken 488 antibody (Jackson ImmunoResearch Laboratories, 703-545-155)
Validation	All primary antibodies have been previously used in several publications: ab167453 - PMIDs: 29556030, 30528281 226003(SY) - PMIDs: 31097621, 31376224 3724S - PMIDs: 26743492, 25077630 ab13970 - PMIDs: 30385274, 30559277

Animals and other organisms

Policy information about studies involving animals; ARRIVE guidelines recommended for reporting animal research

Laboratory animals	For initial torpor experiments we used adult (6-10-week-old) C57BL/6J (The Jackson Laboratory, Stock # 000664) mice. To generate FosTRAP-Gq mice we crossed Fos2A-iCreER (TRAP2) (The Jackson Laboratory Stock # 030323) with R26-LSL-Gq-DREADD (The Jackson Laboratory Stock # 026220) and used adult (6-18-week-old) male and female F1 progeny. For viral injections we

	used Fos2A-iCreER (TRAP2) (The Jackson Laboratory Stock # 030323), Adcyap1-2A-Cre (The Jackson Laboratory Stock # 030155), Vglut2-ires-cre (The Jackson Laboratory Stock # 028863) and Vgat-IRES-Cre (The Jackson Laboratory Stock # 028862) mice.
Wild animals	The study did not involve wild animals
Field-collected samples	The study did not involve samples collected in the field
Ethics oversight	Animal experiments were approved by the National Institute of Health and Harvard Medical School Institutional Animal Care and Use Committee, following ethical guidelines described in the US National Institutes of Health Guide for the Care and Use of Laboratory Animals.

Note that full information on the approval of the study protocol must also be provided in the manuscript.